

## Body-wave passive seismic interferometry revisited: mining exploration using the body waves of local microearthquakes

Polychronopoulou, Katerina; Lois, Athanasios; Draganov, Deyan

**DOI**

[10.1111/1365-2478.12884](https://doi.org/10.1111/1365-2478.12884)

**Publication date**

2019

**Document Version**

Final published version

**Published in**

Geophysical Prospecting

**Citation (APA)**

Polychronopoulou, K., Lois, A., & Draganov, D. (2019). Body-wave passive seismic interferometry revisited: mining exploration using the body waves of local microearthquakes. *Geophysical Prospecting*, 68(1), 232-253. <https://doi.org/10.1111/1365-2478.12884>

**Important note**

To cite this publication, please use the final published version (if applicable). Please check the document version above.

**Copyright**

Other than for strictly personal use, it is not permitted to download, forward or distribute the text or part of it, without the consent of the author(s) and/or copyright holder(s), unless the work is under an open content license such as Creative Commons.

**Takedown policy**

Please contact us and provide details if you believe this document breaches copyrights. We will remove access to the work immediately and investigate your claim.

# Body-wave passive seismic interferometry revisited: mining exploration using the body waves of local microearthquakes

Katerina Polychronopoulou<sup>1,2\*</sup>, Athanasios Lois<sup>2</sup> and Deyan Draganov<sup>3</sup>

<sup>1</sup>Department of Mining Engineering, School of Mining and Metallurgical Engineering, National Technical University of Athens, Athens, Greece, <sup>2</sup>Seismotech S.A., Athens, Greece, and <sup>3</sup>Department of Geoscience and Engineering, Delft University of Technology, Delft, The Netherlands

Received March 2019, revision accepted September 2019

## ABSTRACT

As the global need for mineral resources is constantly rising and the exploitable concentrations of these resources tend to become increasingly complex to explore and exploit, the mining industry is in a constant quest for innovative and cost-effective exploration solutions. In this context, and in the framework of the Smart Exploration action, an integrated passive seismic survey was launched in the Gerolekas bauxite mining site in Central Greece. A passive seismic network, consisting of 129 three-component short-period stations was installed and operated continuously for 4 months. The acquired data permitted detection of approximately 1000 microearthquakes of very small magnitude (duration magnitude ranging between  $-1.5$  and  $2.0$ ), located within or at a very close distance from the study area. We use this microseismicity as input for the application of passive seismic interferometry for reflection retrieval, using the body waves (P- and S-wave coda) of the located microearthquakes. We retrieve by autocorrelation zero-offset virtual reflection responses, per component, below each of the recording stations. We process the acquired results using reflection processing techniques to obtain zero-offset time and depth sections, both for P- and for S-waves. In the context of the present work, we evaluate one of the acquired depth sections, using an existing seismic line passing through the Gerolekas passive seismic network, and we perform forward modelling to assess the quality and value of the acquired results. We confirm that passive seismic reflected-wave interferometry could constitute a cost-effective and environmentally friendly innovative exploration alternative, especially in cases of difficult exploration settings.

**Key words:** Seismic interferometry, Body waves, Local seismicity, Passive method.

## INTRODUCTION

Mining exploration allows the delineation of commercially viable concentrations of minerals or metals for mining purposes, thus ensuring the sustainability of the mining industry itself. Because these concentrations become more and more difficult to explore, as the resources that were convenient to find

and exploit tend to become rarer, the mining industry seeks for alternative, innovative solutions that would contribute in overcoming these difficulties, in an efficient and cost-effective way.

Passive seismic is an exploration approach characterized by both cost-effectiveness and minimum environmental impact. The absence of active sources, either explosives or heavy vibrating machinery, which are necessary for the implementation of any active seismic survey, as well as the

---

\*E-mail: kpolychro@metal.ntua.gr

stand-alone receivers involved, minimize the need for interventions in the landscape and make passive seismic more flexible, mainly in terms of accessibility and environmental impact. It is evident that this flexibility affects positively the cost of passive seismic surveys because, apart from the non-negligible cost of the active sources themselves, passive seismic operations need much smaller crews and lighter vehicles in the field. Of course, one must deal with the fact that passive seismic suffers from the same characteristic that constitutes its major asset: the absence of controlled sources and the consequent uncertainty in the detection and extraction of adequate signals from the continuous passive seismic records.

In that scope, an integrated passive seismic survey was designed and launched in the Gerolekas bauxite mining site, Central Greece, in the framework of the Smart Exploration action. A dense network of stand-alone seismic stations was installed, covering an area of approximately 35 km<sup>2</sup>, and operated continuously during a 4-month recording period. The survey area is mostly unexplored, even though the surrounding area, which constitutes one of the major bauxite-producing sites in Greece, is being exploited for years.

The passive seismic dataset that was acquired is planned to be processed using different passive seismic methodologies, resulting in an integrated subsurface model, based solely on passive seismic data. One of the techniques applied is passive seismic interferometry using body waves for extraction of reflection information below the area of interest.

Seismic interferometry (SI) is a robust methodology that allows the retrieval of the seismic response at a receiver location due to a virtual source located at the same or a different receiver position. It may be applied using two different parts of the seismic signal, either body waves or surface waves, and is characterized as reflected-wave or surface-wave SI, respectively (Wapenaar *et al.* 2010). Reflected-wave SI, which is applied in the present study, is mainly used for imaging the reflectors in the subsurface by exploitation of the body waves present in passive or active seismic signals.

In the context of passive reflected-wave SI, the useful signal (body waves) that is extracted from passive records might have been generated by either noise sources (ambient or anthropogenic) or earthquake activity, either in the area (local seismicity) or at a distance (teleseismic events). However, the majority of the attempts made to extract body waves from continuous passive seismic records, either using wave-separation methodologies (Draganov *et al.* 2013; Almagro Vidal *et al.* 2014; Panea *et al.* 2014; Cheraghi, Craven and

Bellefleur 2015), or using information from regional or even global seismological networks (Scherbaum 1987; Daneshvar, Clarence and Savage 1995; Nakata, Snieder and Behm 2014), has shown that this might be quite a difficult task, especially in cases when the methodology is being applied at an exploration scale. This is due both to the fact that surface waves dominate the majority of the passive seismic records, masking the body-wave content of the noise panels, and to the intrinsic limitation of regional seismological networks, which provide earthquake catalogues including events above a magnitude threshold, thus significantly limiting the number of available exploitable body waves.

Initially introduced by Claerbout (1968) for one-dimensional media and expanded to three-dimensional media by Wapenaar (2004), reflected-wave SI has mainly been applied using controlled sources (Schuster, Yu and Rickett 2004; Minato *et al.* 2011), coda waves of distant earthquakes (Abe *et al.* 2007; Ruigrok, Campman and Wapenaar 2011; Ruigrok and Wapenaar 2012; Nishitsuji *et al.* 2016a,b) and ambient noise (e.g. Draganov *et al.* 2007, 2009; Nakata *et al.* 2011; Boullenger *et al.* 2011; Cheraghi *et al.* 2015; Oren and Nowack 2017; Romero and Schimmel 2018). Attempts to use local earthquakes were rare and mostly based on local seismicity recorded by permanent global or regional networks installed in the broader area of interest (Scherbaum 1987; Daneshvar *et al.* 1995). This fact was significantly limiting the number of available exploitable events, thus having an impact on the obtained results.

However, in the Gerolekas passive seismic study, we take advantage of the area's high level of seismicity, as well as the fact that we are able to accurately detect and locate local microseismic activity, using a dense seismological network. This provided a very robust dataset, consisting of approximately 1000 microearthquakes, located inside or at a very close distance from the survey area. We use this dataset as input for the application of body-wave passive SI.

In the framework of the present work, an overview of the Gerolekas passive seismic survey is presented, followed by a description of the techniques used for earthquake location and application of passive SI using the body waves (P and S) of local microearthquakes. The virtual reflection responses retrieved by this procedure are processed using conventional reflection processing routines, and the obtained results are described and evaluated against legacy active-source data. The evaluation is completed by application of elastic forward modelling, simulating the actual passive-survey conditions, leading to a discussion on the potential of the application of this methodology for mining exploration.

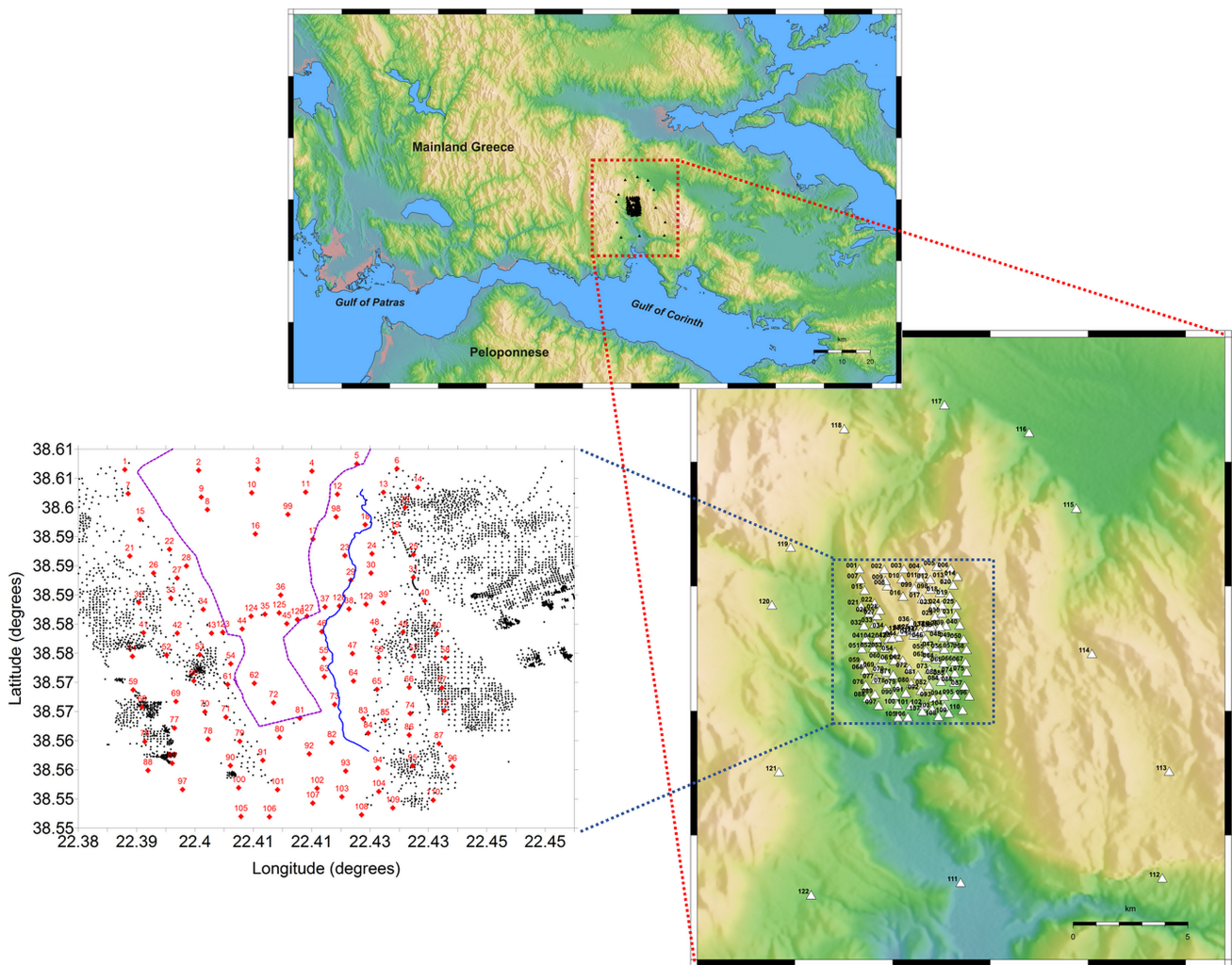


**Figure 1** Location of the Gerolekas study area (top). The red-dotted rectangle corresponds to the study area and is depicted in more detail below (right). White triangles correspond to the 129 three-component short-period seismological stations of the Gerolekas passive seismic network. The blue-dotted rectangle, corresponding to the Gerolekas mining site, is depicted in more detail on the left. Red diamonds correspond to the inner network's station locations, whereas black dots represent the more than 4000 wells, drilled by the mining company, delineating the extent of the exploited part of the mining site. The blue line shows the location of the legacy seismic section PARV-1. The Gerolekas nappe's limits, as delineated by surface geology, are noted by a magenta dashed line.

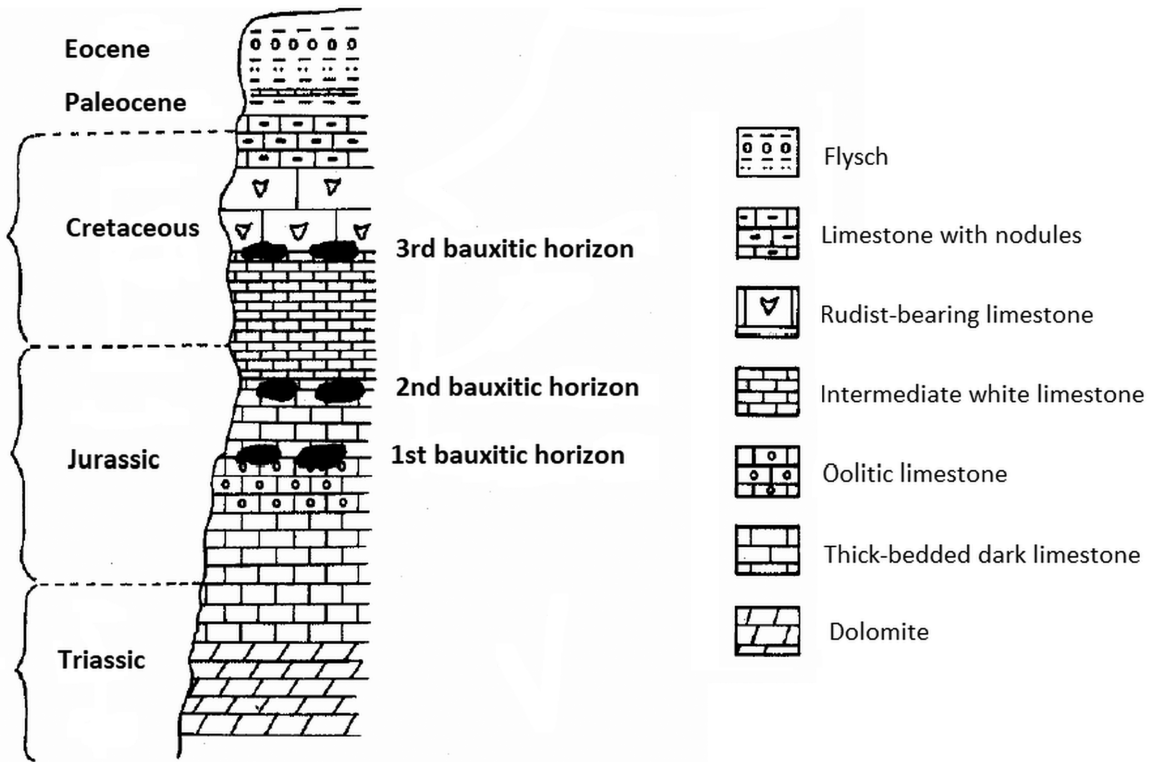
## OVERVIEW OF THE GEROLEKAS PASSIVE SEISMIC SURVEY

The Gerolekas mining site is located between the Giona and the Parnassus mountains, in Central Greece (Fig. 1). It belongs to the geotectonic zone of Parnassus–Giona, which is characterized by a relatively simple stratigraphy, consisting of a sequence of carbonate rocks underlying a flysch horizon. A simplified stratigraphic column of the Parnassus–Giona zone is presented in Figure 2 (top). It shows the dolomites of the Middle Triassic, followed by a succession of limestones, dating from the Upper Triassic (thick-bedded dark

limestones) to the Jurassic (oolitic limestones underlying a series of intermediate white limestones) and the Cretaceous period (intermediate white limestones, rudist-bearing limestones and limestones with nodules). This sequence of carbonate rocks is covered by Paleogene flysch.

Bauxite deposits exist in the area and appear as layers or lenses hosted within the carbonate rocks (Fig. 2). They are considered to be allochthonous (Aronis 1955), as they were the product of the laterization of ophiolites found in eastern Greece, which were transported and deposited into karstic cavities of the underlying limestone in the Parnassus region.

### Stratigraphy of the Parnassus - Giona zone



### Simplified Gerolekas stratigraphy

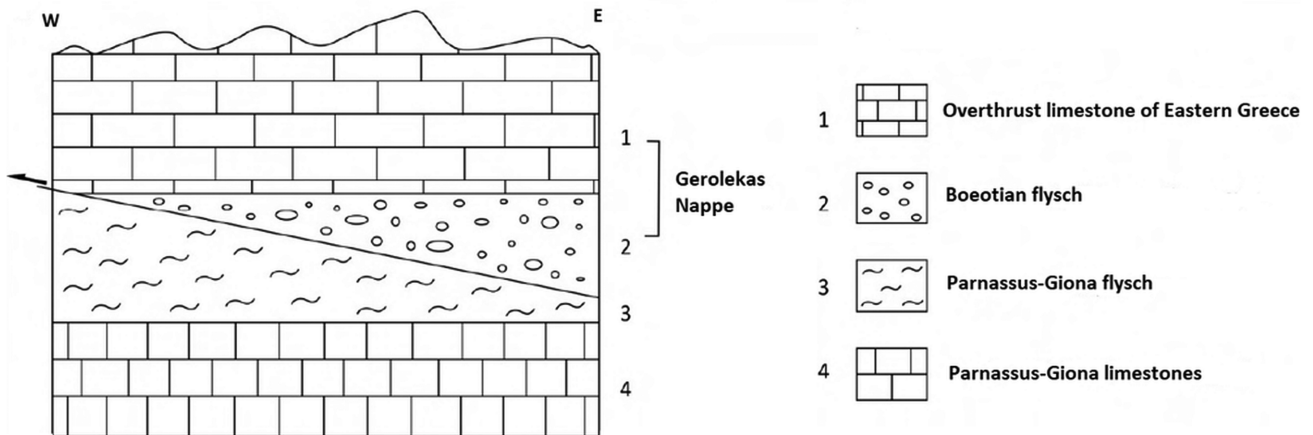
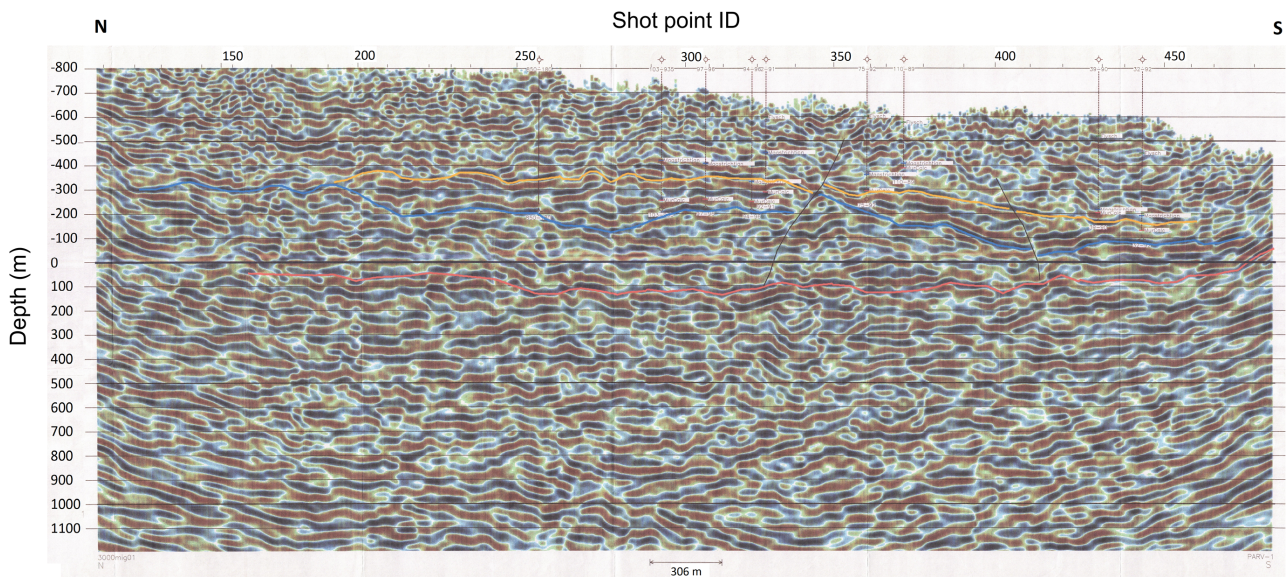


Figure 2 Stratigraphic column of the Parnassus-Giona zone (top) and simplified sketch of the Gerolekas stratigraphic overlap (bottom).

This procedure, which took place during different geological periods, resulted in the formation of three distinct bauxitic horizons (Benardos and Katopodis 2011). As it can be observed in Figure 2, the first two horizons lay between the oolitic limestones of the Middle Jurassic and the intermediate white limestones of the Upper Jurassic, whereas the third

horizon is hosted between the limestones of the Middle and Upper Cretaceous. From the three bauxitic horizons present in the area, the upper two are exploitable (second and third bauxitic horizon), whereas the uppermost (third bauxitic horizon) is of diasporic type and characterized as the most important in terms of mining interest.



**Figure 3** Migrated depth section PARV-1. The seismic line extends from the surface (datum at 800 m above mean sea level) down to a depth of 1200 m below mean sea level. Three major reflectors have been interpreted, delineated by the three coloured lines (yellow, blue and red) on the seismic section. (Courtesy of Delfi-Distomon S.A.)

The broader area is affected by intense thrust and reverse faulting, as well as fault-bend folds, mainly due to the alpine orogenic cycle, which are responsible for the existence of numerous stratigraphic overlaps. This is expected to be the case of the Gerolekas stratigraphy as well. More specifically, the Gerolekas area is characterized by a stratigraphic overlap of a sequence consisting of Triassic limestones overlying Boeotian flysch, coming from eastern Greece, that has been tectonically emplaced on the Parnassus–Giona flysch. A simplified sketch of the Gerolekas stratigraphy is depicted in Figure 2 (bottom).

Although the area surrounding Gerolekas has been extensively explored and exploited by the bauxite mining company operating in the area (Delphi-Distomon S.A., Amfissa, Greece), the Gerolekas site still remains completely unexplored, mainly due to its rough topography and limited accessibility (Fig. 1). The only exploration attempt made was a geophysical study that was launched in 2003, consisting of the acquisition of three lines of two-dimensional conventional seismic and gravity data, along the edges of the Gerolekas nappe. However, this survey was not designed to provide any insight about the subsurface below the main body of the Gerolekas site, leaving the question of the vertical extent of the nappe still unanswered.

One of the acquired seismic sections was the line PARV-1. This section was shot in 2003 by Hellenic Petroleum, in the context of a broader geophysical study launched

by Delfi-Distomon S.A. The legacy migrated depth section PARV-1 is presented in Figure 3.

The total length of seismic section PARV-1 was approximately 6 km, whereas the depth of the migrated depth-converted section was 2 km (Fig. 3). Its datum was set at 800 m above mean sea level. Based on the interpretation of PARV-1, three major reflectors were detected on the migrated depth section. These reflectors are delineated by the three lines (yellow, blue and red) drawn on PARV-1 and were interpreted as geological contacts between the flysch and the underlying limestone or between the different phases of flysch.

Taking into account the fact that bauxite deposits in the surrounding area have already been appraised by the mining company, as well as the fact that, so far, no information is available on the subsurface below Gerolekas, exploration of this part of the mining area is crucial for the planning and sustainability of future mining activities in the area.

The most important question that we need to answer is the depth at which the flysch-limestone contact is located below the Gerolekas nappe. This information is of major importance for the mining company, because it will define the exploitability of possible bauxite reserves that are expected to be located slightly below this contact (Fig. 2). Having in mind that the mining company was looking for a cost-effective and environmentally friendly exploration solution, flexible enough to overcome the accessibility issues of the Gerolekas

area, a passive seismic survey was designed and launched in the Gerolekas bauxite mining site.

More specifically, a network of three-component short-period seismological stations was installed, covering an area of approximately 35 km<sup>2</sup>. This network consisted of 129 stand-alone stations –117 were installed on a relatively regular grid of 500 × 500 m (Fig. 1), covering the area of interest, whereas 12 were installed as peripheral stations, aiming at ensuring a better control of the recorded seismicity, mainly in terms of azimuthal coverage. All seismological stations were equipped with the same three-component geophone-based force-balance seismic sensors, with a bandwidth between 0.2 (–6 dB) and 98 (–3 dB) Hz and a flat response between 1 and 60 Hz.

The stand-alone stations, as well as the local soil conditions that permitted a good coupling with a superficial installation of the seismic sensors, contributed to overcoming accessibility issues, which were for years the major deterrent to exploring this part of the mining site. Opposed to active seismic surveys, the stand-alone stations of a passive seismic network are installed at fixed locations and left recording during a specific period of time. Data are collected at pre-defined intervals and sent for processing. Installation of the Gerolekas passive seismic network was completed in approximately 1 week and the network was continuously operating during a 4-month recording period (May–August 2018). Data collection was realized at 15-day intervals.

## THE DATASET

Once we acquire each set of raw data from the field, we initially prepare them for processing. The initial preparation consists in removing the signals' dc component, by subtracting their mean values (zero-mean signals), and then filtering using a bandpass filter at the frequency band of interest. In this case, we filter at 1–45 Hz, because we record at 100 samples per second, thus having a Nyquist frequency of 50 Hz, and our target is to exploit microearthquakes with a frequency content significantly higher than 1 Hz. Because all stations are equipped with the same sensors, we do not apply instrument response correction. We then analyse the pre-processed continuous records to locate microseismic events that occurred during the acquisition period within the extent of the installed network or at a very close distance (<5 km) from it.

Event detection is performed automatically, using an energy-based algorithm (Leontarakis *et al.* 2015) with an improved short-time-average/long-time-average (STA/LTA) detector that uses information from all three components of each record, instead of exploiting only the vertical component

of the signal, as in the classical STA/LTA approach. In this energy-based approach, the declaration of a candidate seismic event is performed by means of comparison of the ratio of two windows moving along the signal with a dynamic threshold based on the statistical characteristics of the ratio sequence. It must be noted here that in order for a candidate event to pass the detection criteria, the above-mentioned condition must be fulfilled in a sufficient number of neighbouring stations. This is achieved by multi-station analysis, taking into account the geometry of the installed network.

We then isolate the detected signal segments from the continuous records and the P- and S-waves' onset time is automatically estimated. The estimation is based on the statistical characteristics of the detected signals. More specifically, the P-wave onset time is assigned to the point where the fourth-order zero-lag cumulant of a seismic signal, kurtosis (Saragiotis, Hadjileontiadis and Panas 2002), presents its maximum slope. The estimation of the S-wave onset time is based on eigenvalue analysis of the three-component signal, which results in a characteristic function corresponding to the maximum eigenvalue sequence. In that case, the kurtosis criterion is applied on this characteristic function, resulting in an accurate estimation of the S-wave onset time (Lois *et al.* 2013).

This procedure results in a list of detected seismic events, along with the corresponding P- and S-wave first arrival times. These times are then used to estimate the hypocentral location of the events, leading to a catalogue of local microseismicity.

In the case of the Gerolekas passive seismic survey, approximately 3000 earthquakes, with duration magnitude (Md) ranging between –1.5 and 2.5 approximately, are located in the broader area following the above-described procedure. Md is based on the duration of the earth's movement, as measured by the time decay of the amplitude of the seismogram and is often used when measuring very small events. From those events, 954 are located at epicentral distances of less than 5 km from the nearest station (Fig. 4) and characterized by specific quality criteria (their location is based on more than 10 P- and S-wave arrival times, the root-mean-square error of their location solution is less than 0.15, and the horizontal and vertical uncertainty of their hypocentral locations is less than 1 km). Their Md ranges between –1.5 and 2.0. We further use the P- and S-wave coda of these 954 local microearthquakes as the input for reflected-wave seismic interferometry processing.

We construct a Wadati plot using the located events (Fig. 5). A Wadati plot depicts the observed P-wave arrival time versus the observed S-P interval (Wadati 2011). The gradient of its trend line provides an estimate of the global  $V_p/V_s$

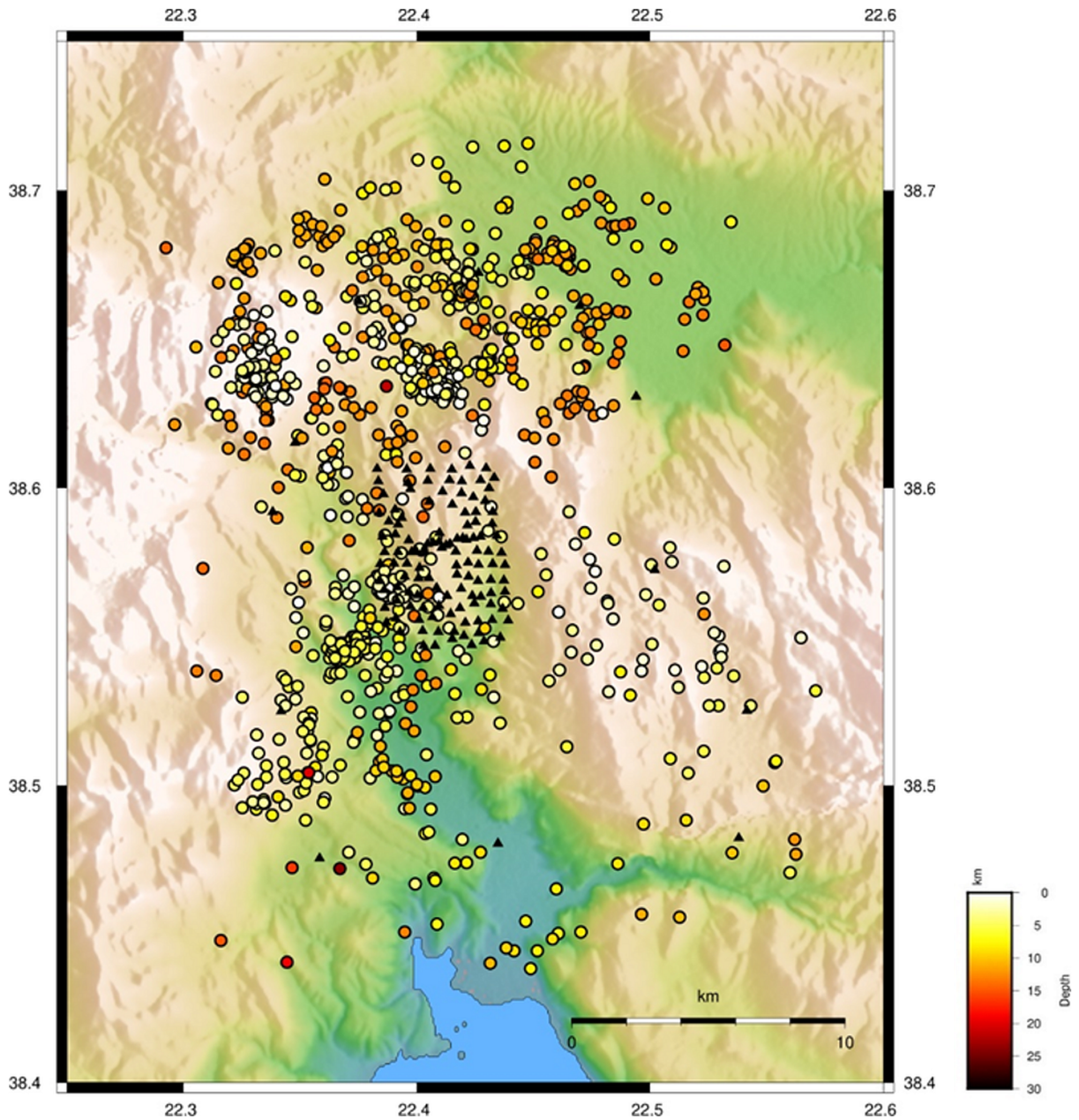


**Figure 4** Seismicity located at a maximum epicentral distance of 5 km from the nearest station of the Gerolekas passive seismic network during the four-month recording period. It consists of 954 microearthquakes, which are depicted by colour-coded dots on the map. The colourscale corresponds to the earthquakes' hypocentral depths. The black triangles correspond to the network's station positions.

value of the study area. The underlying assumption is that the area can be characterized by a global  $V_p/V_s$  value, if the Wadati plot is nearly linear. In that case, the  $V_p/V_s$  ratio can be estimated using

$$\frac{V_p}{V_s} = \frac{t_s - t_p}{t_p - t_0} + 1, \quad (1)$$

where  $t_p$  and  $t_s$  are the P- and S-wave onset times, respectively,  $t_0$  is the microearthquake's origin time, as estimated during event location, and the ratio  $\frac{t_s - t_p}{t_p - t_0}$  corresponds to the Wadati-plot gradient.

In the case of the Gerolekas survey, the Wadati plot of Figure 5 is far from being globally linear, insinuating significant variations in the local  $V_p/V_s$  ratio. Further analysis is



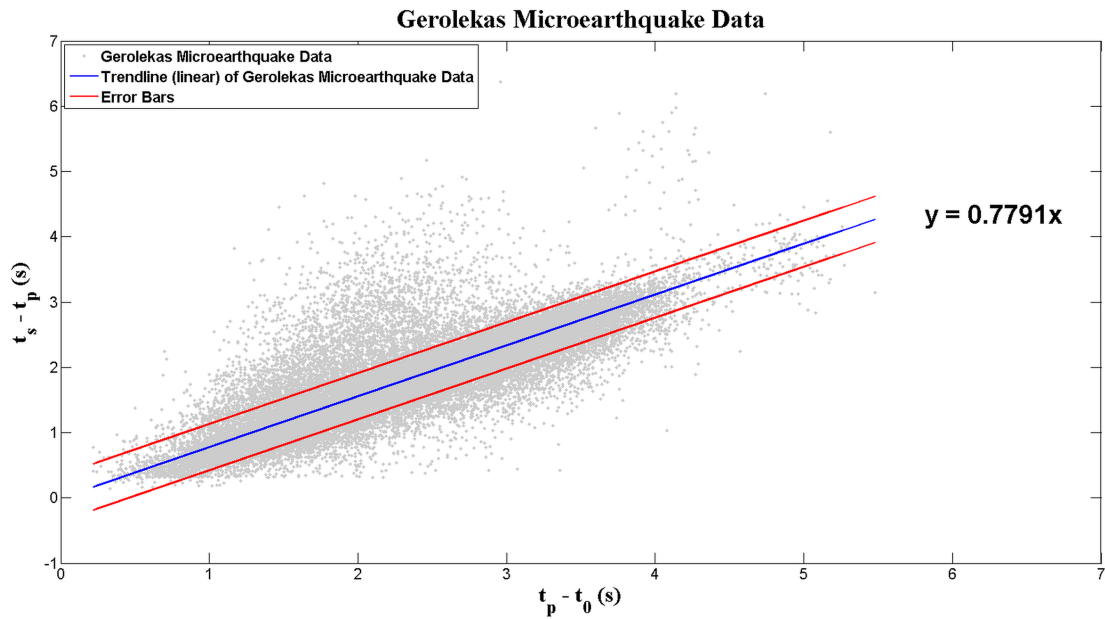


**Figure 5** Wadati plot of the Gerolekas microearthquake dataset. The observed P-wave arrival time ( $t_p - t_0$ ) is plotted versus the S-P interval ( $t_s - t_p$ ). The fitted linear trend of the plotted arrival times provides an indication of the average  $V_p/V_s$  ratio characterizing the study area. Here, a global value of  $V_p/V_s$  equal to 1.78 is estimated.

required in order to conclude on the parts of the study area that are characterized by different  $V_p/V_s$  ratio values, affecting the Wadati plot results. However, because our scope is to be able to estimate a global  $V_p/V_s$  ratio value that will permit the calculation of a one-dimensional S-wave velocity model for data processing, an average  $V_p/V_s$  ratio of 1.78 can be assumed, by fitting a trend line of the scattered data and taking into account the relevant uncertainty.

## PASSIVE SI USING BODY WAVES OF LOCAL EARTHQUAKES

In the context of the present work, we are focusing on the application of reflected-wave seismic interferometry (SI) using the P- and S-wave coda of the local microearthquakes.

By selecting those recordings of the dataset of 954 microearthquakes that were reaching a station nearly vertically, we can apply the theory of reflected-wave SI to retrieve the zero-offset seismic reflection response below the station under consideration from a virtual source co-located with the station and emitting energy nearly vertically down. Thus, assuming a horizontally layered subsurface below each station and illumination from below by a vertical plane wave, we can apply the following relation (Claerbout 1968; Wapenaar *et al.* 2010):

$$R(t) + R(-t) = \delta(t) - T(t) \times T(-t), \quad (2)$$

where  $R(t)$  is the global reflection response of a downgoing, vertical plane wave illuminating the medium from the free surface,  $T(t)$  is the global transmission response of a vertically propagating plane wave observed at the free surface and the Kronecker  $\delta(t)$  represents the pulse of the illuminating wavefield. By this relation, it becomes evident that the global reflection response below a recording station can be obtained from the autocorrelation of the global transmission response and that the causal part of the autocorrelation is equal to  $-R(t)$ , whereas the acausal part is equal to  $-R(-t)$ .

As in reality the horizontally layered earth assumption is often not fulfilled and the transmission responses are often affected by the distribution of the sources and their time functions, their autocorrelation results in the retrieval of both physical and non-physical (spurious) events. A way to deal with this fact is by calculating the autocorrelation for an adequate number of different plane waves and stacking the results. In that sense, the physical events are enhanced, whereas the spurious ones are eliminated. Therefore, for the  $i$ th station of a passive seismic network, equation (2) can be extended to

$$R^i(t) + R^i(-t) = \delta^i(t) - \sum_n T_n^i(t) \times T_n^i(-t), \quad (3)$$

where  $\sum_n T_n^i(t) \times T_n^i(-t)$  is the summation (stacking) of the autocorrelations of the global transmission responses of the

(nearly) vertically propagating plane waves of  $n$  different earthquakes recorded at station  $i$ . Because these earthquakes have occurred at different times and locations, they can safely be considered as independent sources, the stacking over which enhances the coherent energy included in the autocorrelation function of their global transmission responses and eliminates random noise and spurious events.

By applying this procedure, a zero-offset reflection response is acquired at the position of each of the recording stations. Note that sources located at the edges of the spatial extent must be tapered. Although this is possible when using microearthquakes, it would add extra processing time. Thus, we do not do it. As a consequence, artefacts would arise in the retrieved result, which would manifest themselves in lowering the signal-to-noise ratio of the interpretable physical events. The above equations are true strictly for acoustic medium. In elastic medium, their application will result in retrieval of artefacts due to correlation between P- and S-wave arrivals recorded by the same component. By choosing the microearthquake sources to result in recorded signals with near-vertical incidence, we effectively minimize the creation of cross-component artefacts, because wave conversions are minimal at near-vertical incidence.

Based on the above-mentioned methodology, we develop the processing workflow presented in Figure 6, which we apply on the Gerolekas dataset. More specifically, in the case of the Gerolekas survey, we first assess the 954 microearthquakes located within the broader area of interest, in terms of verticality of the rays of the first arrivals (both P and S) at each station. This is demanded by the application of equation (2) for retrieval of zero-offset reflection response from a virtual source emitting energy vertically down. In order to do this, we calculate the hypocentral distances from each station and we assume that a recorded seismic signal is nearly vertical when the angle of the ray travelling from the hypocentre towards a station from the vertical is less than  $20^\circ$ . This procedure resulted in a dataset of 562 microearthquakes that arrived nearly vertically at least at one station. We then organize these earthquakes per station, defining the signals that would be used in the context of the estimation of the virtual reflection response below each station, by applying equation (3). An example of the events used for station 1 of the Gerolekas passive seismic network is depicted in Figure 7, whereas a density plot of the number of microearthquakes that contributed in the calculation of the autocorrelation function below each station is presented in Figure 8.

In the next step, we extract the useful signal from the continuous records. To that end, the P- and S-wave arrival times

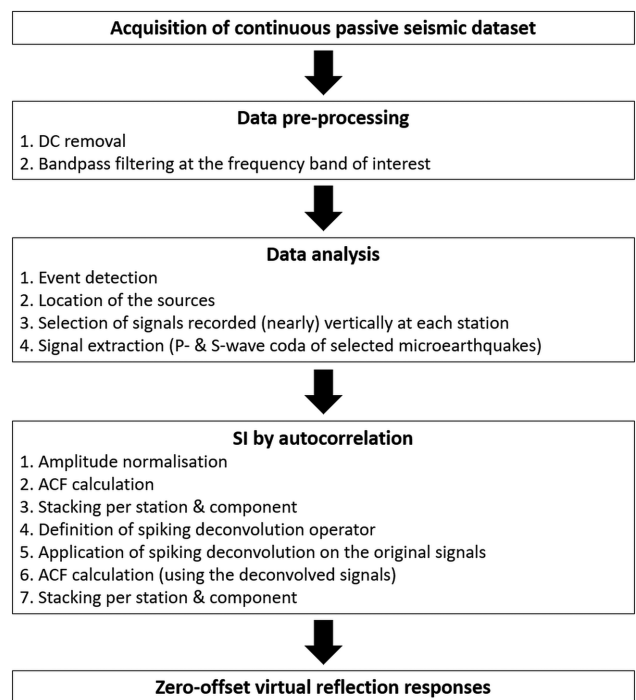


Figure 6 Processing workflow for the application of SI by autocorrelation on microearthquake data.

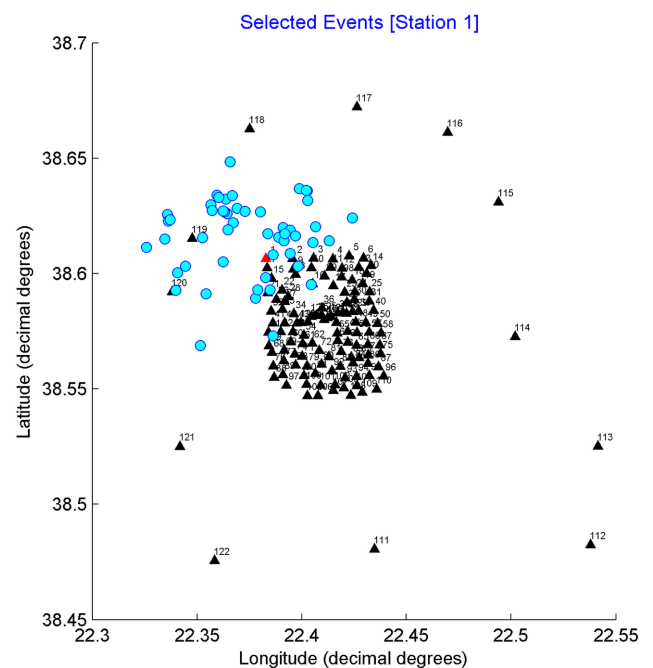


Figure 7 Exploitable seismicity for passive seismic interferometry at station 1 (red triangle). It consists of 51 microearthquakes, whose first arrivals are vertical or nearly vertical at station 1. Station locations of the Gerolekas passive seismic network are denoted by black triangles. Epicentres of the selected earthquakes are depicted using blue circles.

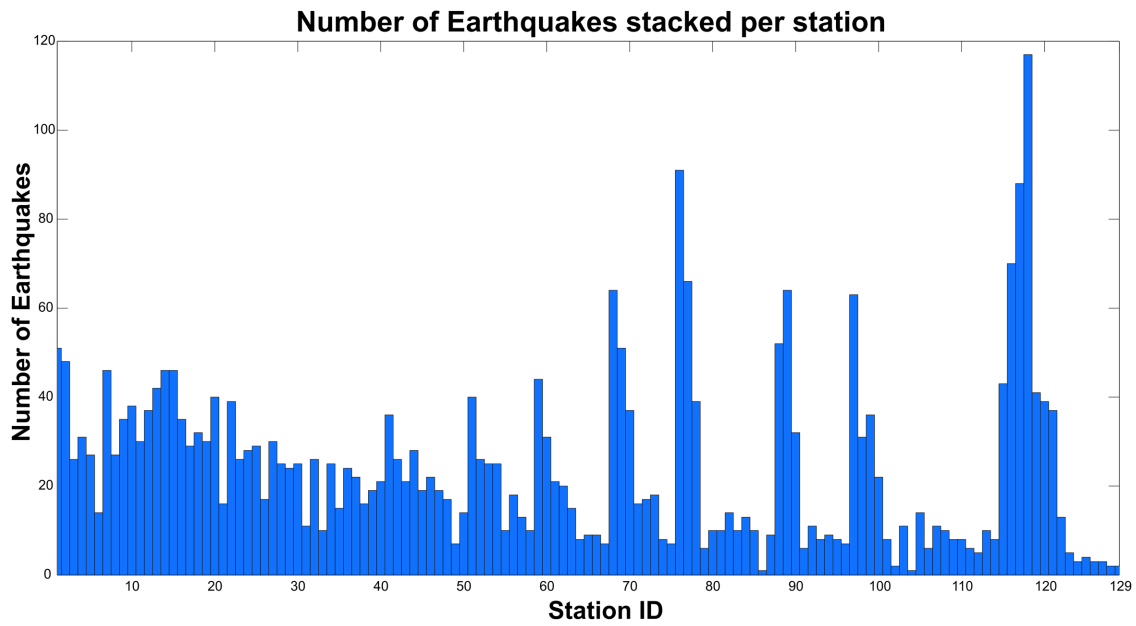


Figure 8 Density plot of the number of exploitable microearthquakes recorded at each station of the Gerolekas passive seismic network. These microearthquakes, the first arrivals of which arrive vertically or nearly vertically at the relevant station, are used for calculation of the autocorrelation function below the station under investigation.

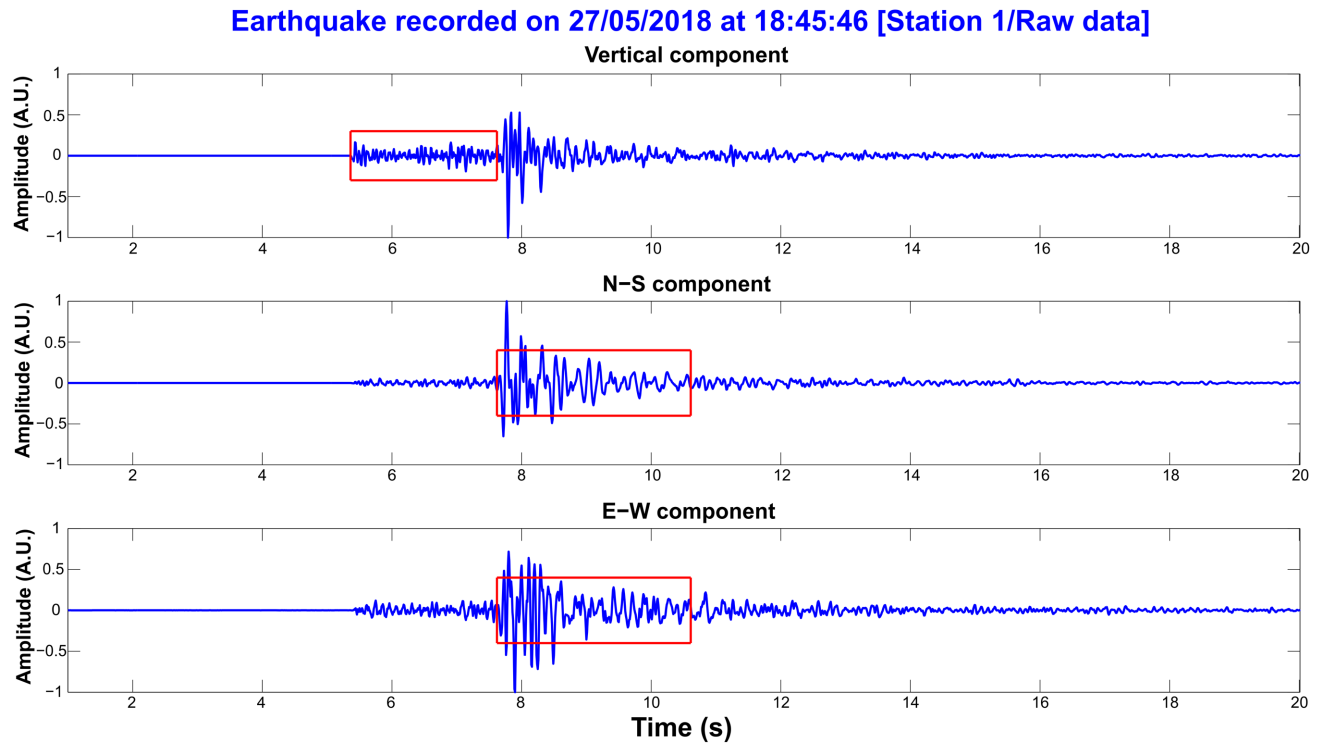
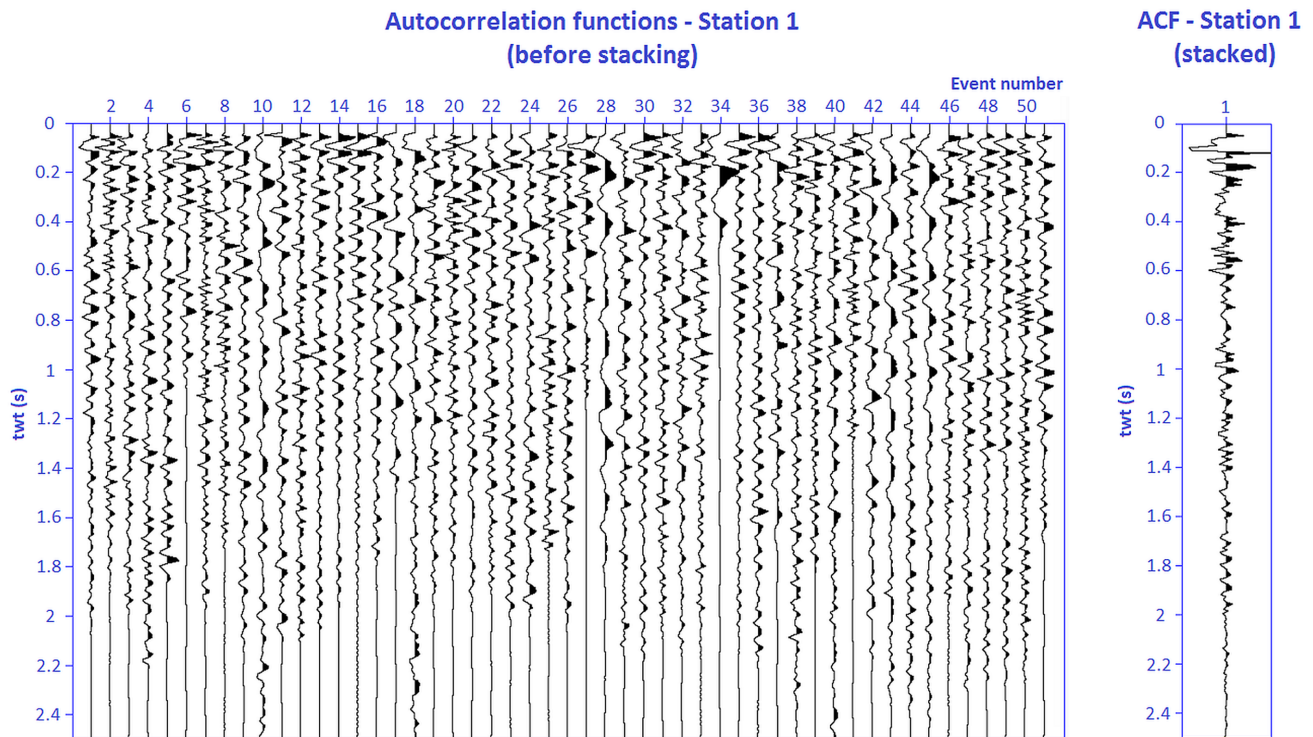


Figure 9 Earthquake recorded on the 27th of May, 2018, at 18:45:46. Raw data recorded by the three components (vertical component: top/N-S component: middle/E-W component: bottom) of station 1 of the Gerolekas passive seismic network. The red rectangle corresponds to the window used for the extraction of the P- (vertical component) and S-wave coda (horizontal components), including the corresponding direct arrivals.



**Figure 10** Autocorrelation functions calculated for the 51 microearthquakes satisfying the verticality criterion for station 1 of the Gerolekas passive seismic network before stacking (left) and the output of the summation process (right).

estimated during the event-detection and phase-picking procedures, are used to define the part of the microearthquakes' signal that would be exploited. More specifically, for the signals that passed the verticality criterion set at the previous stage, the P-wave coda is extracted from the vertical component recordings, using a window equal to the S-P time of each record, whereas the S-wave coda is extracted from the horizontal components, along two different directions (North–South and East–West), using the same time window. It must be noted here that even though the P-wave coda window is accurately defined by the P- and S-wave first arrival times, the selection of the S-wave coda window is characterized by more uncertainty. Its definition is based on the assumption that the S-wave coda duration of each of the exploited microearthquakes should be magnitude-dependent and not very different from its P-wave coda duration. According to Perron *et al.* (2018), the S-wave coda window length of an earthquake can be estimated using a function of the difference between the P- and S-wave onset times ( $T_p - T_s$ ). This function consists of the propagation term ( $T_p - T_s$ ), added to a term related to the source's duration, which for small and moderate earthquakes (of  $M < 5$ ) can be neglected. As a result, the S-wave coda duration can be assumed to be similar to the calculated

P-wave coda duration for the microearthquakes involved in the present work ( $M_d < 2$ ). The extracted signals, from the vertical and the horizontal components include the direct P- and S-wave arrivals, respectively. An example event is presented in Figure 9.

Once the useful signals have been selected and extracted from the continuous passive seismic recordings, we amplitude-normalize them and calculate their autocorrelations. We apply amplitude-normalization by dividing each trace by the maximum of the absolute value of the amplitudes within the extracted window. This procedure equalizes the amplitudes of the signals from each microearthquake that will contribute during the summation process, thus securing that each signal's contribution will be independent of the order of magnitude of the amplitudes of the original signal. After that, we stack per component the autocorrelations of the extracted signals recorded at each station and use the resulting stacked autocorrelograms to define a spiking deconvolution operator, using the Levinson–Durbin recursion algorithm (Ljung 1987). An example of the autocorrelation functions calculated for the 51 microearthquakes satisfying the verticality criterion for station 1, before stacking, is presented in Figure 10, along with the output of the summation process.

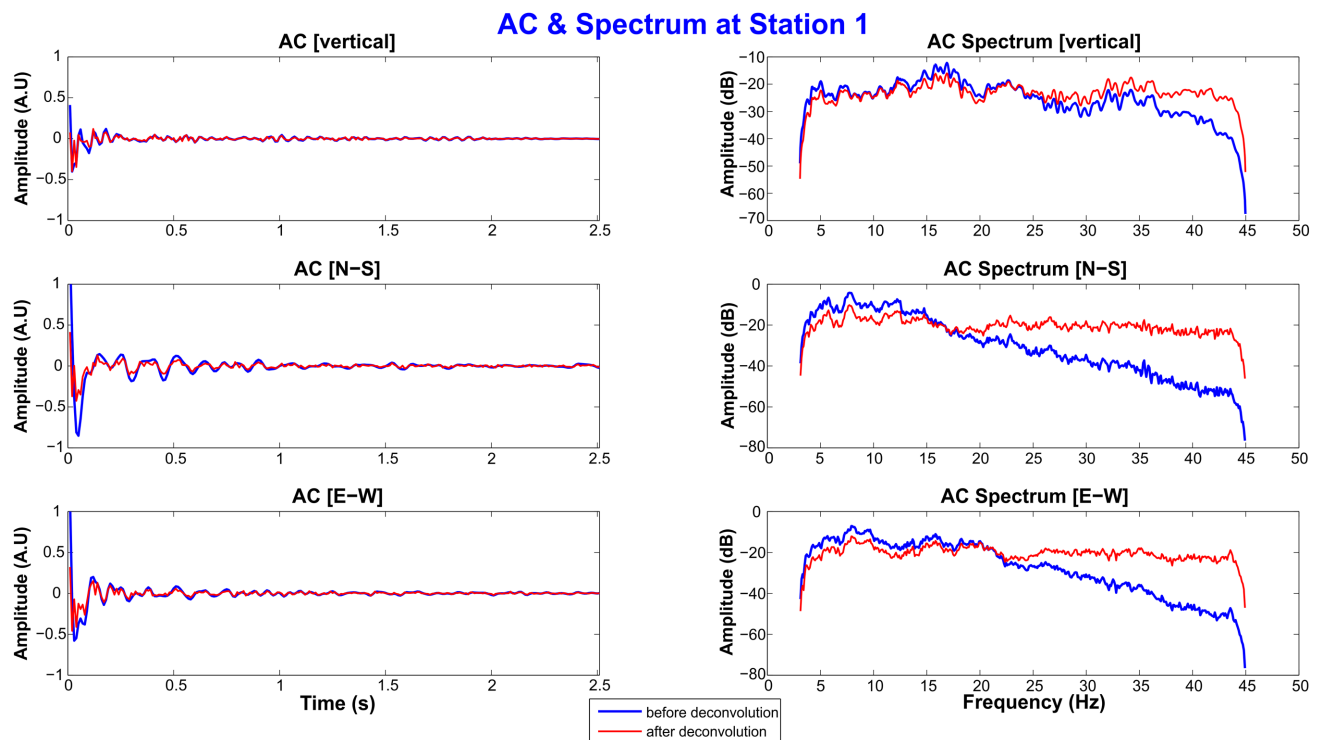


Figure 11 Autocorrelograms and their spectra before and after deconvolution. The autocorrelograms are calculated using the selected signals along the three components of station 1 (vertical component: top/N-S component: middle/E-W component: bottom) of the Gerolekas passive seismic network.

Having in mind that the 51 microearthquakes are located at different positions around station 1 (Fig. 7), providing a good azimuthal coverage of the station by sources, summation of the calculated autocorrelograms should, according to the theory, result in enhancing all the coherent physical events and suppressing non-physical information. All autocorrelation functions of Figure 10 are bandpass filtered between 3 and 45 Hz, in order to eliminate any low-frequency effect. Following, we apply spiking deconvolution on the original signals. This aims to enhance their vertical resolution, by flattening the spectrum in the interval of interest. We then re-calculate autocorrelations of the deconvolved signals and stack again per component at each station, repeating the procedure for all stations.

The above-described procedure results in 129 stacked autocorrelograms of the deconvolved signals per component, corresponding to the virtual P- and S-wave reflection response below each of the 129 recording stations. An example of the stacked autocorrelation functions before and after deconvolution, bandpass filtered between 3 and 45 Hz, is presented in Figure 11. These autocorrelations are calculated using the signals of the 51 microearthquakes, recorded by station 1,

from Figure 7. Observing the two autocorrelograms, it becomes evident that the deconvolution procedure has resulted in an enhanced vertical resolution (along the time axis) for all three components, whereas their spectrum shows that there has been a significant boost on the high-frequency content of the signal. The obtained final summed results at each station correspond to the zero-offset virtual reflection response that would be acquired, if there were a source and a receiver at the station's location, where the source was emitting energy vertically down.

## SEISMIC PROCESSING OF THE VIRTUAL REFLECTION RESPONSES

After retrieving the virtual reflection responses calculated below each station of the Gerolekas network, we process them using part of the standard seismic-exploration processing workflow, in order to acquire zero-offset seismic sections of the subsurface, along various directions. The fact that the virtual reflection responses are zero-offset traces facilitates this procedure, by minimizing the processing steps that need to

## Zero-offset time sections

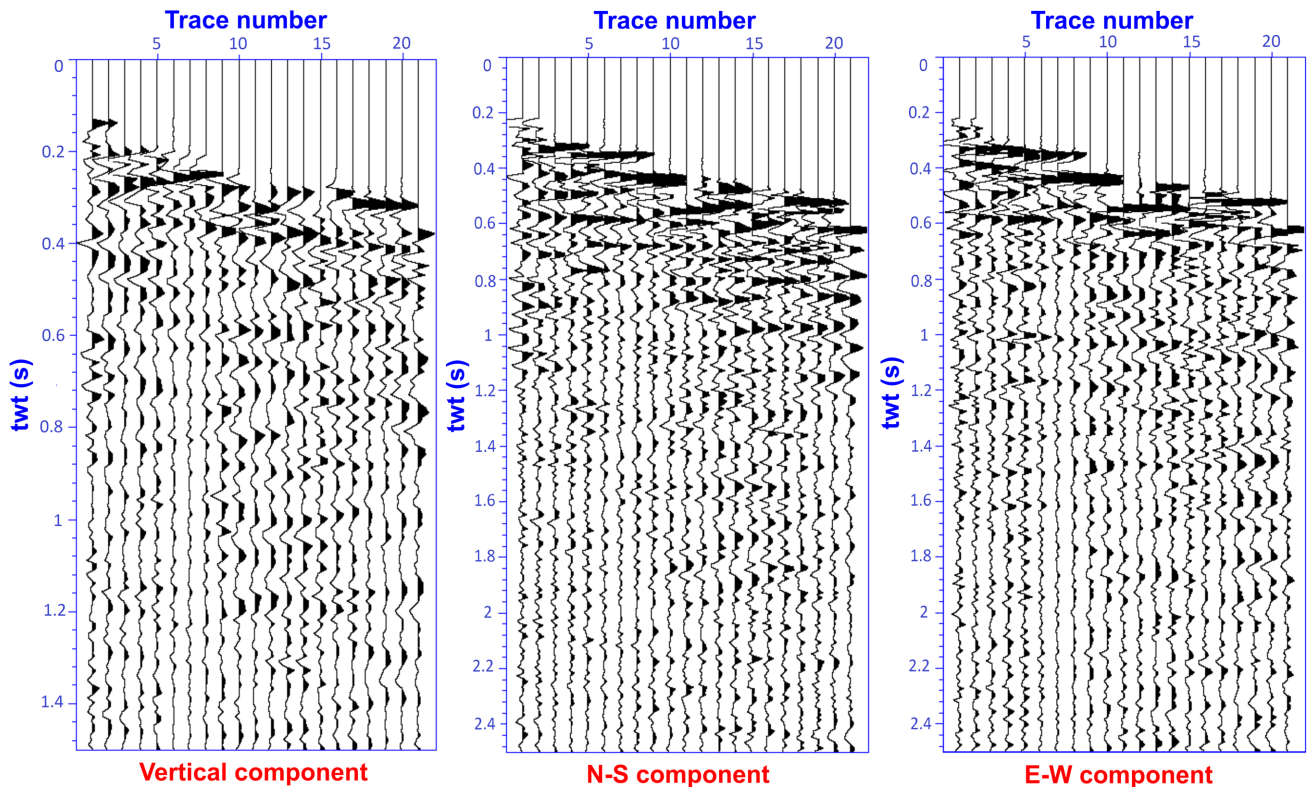


**Figure 12** Zero-offset virtual reflection responses along line PARV-1. Time sections obtained from the autocorrelograms calculated using the P-wave coda, recorded by the vertical component (left), the S-wave coda along the N-S direction (middle) and the S-wave coda along the E-W direction (right), as recorded by the relevant horizontal components.

be applied. We perform seismic processing using CWP/SU: Seismic Un\*x (Stockwell and Cohen 2008).

We only process the virtual reflection responses corresponding to the stations of the inner network (Fig. 1). These stations are characterized by inter-station distances of approximately 500 m, covering an area of  $5 \times 7$  km. Time sampling of all the zero-offset virtual reflection responses is determined from the sampling rate of the raw data at 100 samples per second, while each trace's length is variable and defined by the maximum length of the P- or S-wave coda used during processing. For example, in the case of station 1, the maximum length of the P-wave coda used for calculation of the autocorrelation functions is 2.0 seconds approximately (see Fig. 10).

The first step is to select neighbouring stations, along different directions, forming cross-sections that would be used as input for seismic processing. We select a North–South cross-section, coinciding with the location of PARV-1 seismic profile of the legacy active-source seismic survey. We do this

because this selection provides a possible means of evaluating the obtained results. The location of PARV-1, as well as the inner Gerolekas passive seismic network, is presented in Figure 1, whereas the P- and S-wave zero-offset virtual reflection responses calculated along this cross-section are depicted in Figure 12.

After selecting the desired stations, we process the zero-offset virtual reflection responses by first multiplying them by  $-1$ . This is needed because the calculated autocorrelations are equal to the negative of the global reflection response of the subsurface. After that, we apply static corrections, using the upper part of the models in Figure 13, and the effect of the rough topography, which ranges from 500 m to 1200 m along PARV-1, is taken into account. Finally, we apply time-to-depth conversion to the resulting time sections.

In order to apply both static corrections and time-to-depth conversion, we use an average one-dimensional P-wave velocity model (Fig. 13) derived from the application

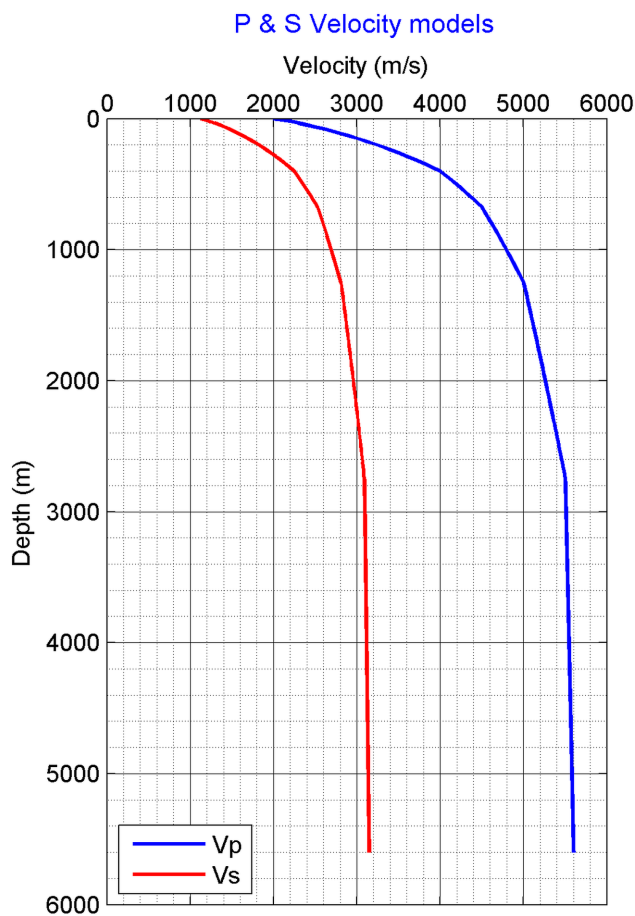


Figure 13 P- and S-wave velocity models used for the time-to-depth conversions and static corrections. The P-wave velocity model ( $V_p$ ) is calculated using local-earthquake travel-time tomography, whereas the S-wave velocity model ( $V_s$ ) is estimated from the P-wave velocity distribution using a  $V_p/V_s$  ratio of 1.78 (Wadati plot in Fig. 5).

of local-earthquake travel-time tomography on the same dataset (Polychronopoulou *et al.* 2019). A more accurate conversion could be achieved by using the three-dimensional model calculated by local-earthquake tomography, but this procedure extends beyond the scope of the present study.

For the S-wave velocity model required for the static corrections and time-to-depth conversion of the S-wave virtual reflection responses, we use the  $V_p/V_s$  ratio of 1.78, estimated from the Wadati plot (Fig. 5).

The resulting depth sections are presented in Figure 14. All cross-sections provide information from the surface (500–1000 m above mean sea level) down to a depth of 5 km below mean sea level. The seismic traces are normalized by their maximum value and interpolated for visualization purposes.

## EVALUATION OF THE VIRTUAL REFLECTION RESPONSES

In order to evaluate the acquired passive seismic interferometry (SI) results, we initially proceed in checking their quality and value by means of forward modelling. We perform two-dimensional (2D) elastic modelling, along the cross-section PARV-1, using a finite-difference modelling code (Thorbecke and Draganov 2011). In that way, we calculate the wavefields that would be produced by a number of passive seismic sources, placed at depth, recorded by a receiver installed at the surface. We then calculate the autocorrelation functions of these wavefields and stack the resulting signals, thus simulating the zero-offset virtual reflection response that would be acquired, if there were a source and a receiver at the station's location, where the source were emitting energy vertically down.

More specifically, we initially create 2D P- and S-wave velocity models, based on all available information on the survey area's subsurface. We take into account geological information and well data from the surrounding area, as well as the original interpretation of the legacy seismic data (Fig. 3). The conceptual  $V_p$  distribution used for the modelling is presented in Figure 15. It consists of a shallow layer of flysch ( $V_p$  of 3000 m/s), because PARV-1 is located outside of the area affected by the Gerolekas nappe (Fig. 1), followed by a succession of limestones ( $V_p$  ranging from 4000 to 5500 m/s). Special emphasis should be given to the thin layer of limestone (vertical extent of 100 m and  $V_p$  of 4000 m/s), located directly below the flysch, which was added to the model in the scope of examining the effect it has on the resulting wavefields, as the existence of such layers has been confirmed by neighbouring wells. For the S-wave velocity model, we use the same spatial distribution as for the P-wave velocity, and we calculate the velocity values using the  $V_p/V_s$  ratio estimated using the Wadati plot of Figure 5. We also include topography in our models, because there is an altitude difference of approximately 700 m along the line PARV-1.

Aiming in keeping the forward-modelling procedure as close to the real conditions as possible, we select the receivers of the Gerolekas passive seismic network that are located along the line PARV-1 and use their real positions. We then extract from the real dataset of the recorded local microearthquakes the locations of those that satisfy the verticality criterion at each of the selected stations. We use these earthquakes as passive seismic sources in order to perform the forward modelling. The locations of the passive sources used for all the modelled stations are presented in Figure 16. It must

### Zero-offset depth sections

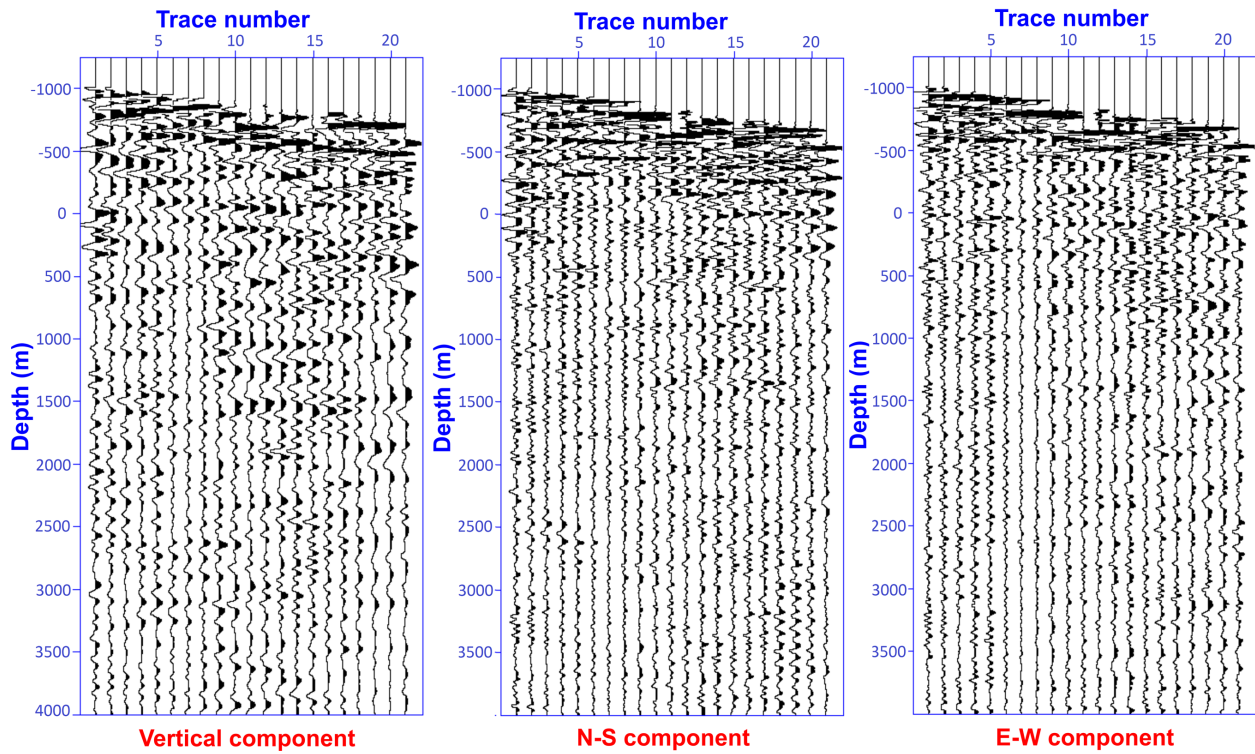


Figure 14 Virtual reflection zero-offset sections along the line PARV-1. Depth sections calculated using the P- (vertical component/left) and S-wave coda (horizontal components/N-S in the middle and E-W on the right) of local microearthquakes.

be noted here that our sources are located at depths ranging between 2.5 and 25 km, with the majority of them laying at a depth of approximately 15 km. However, in order to keep

the model space limited (for faster modelling), we adapt their x and z location by dividing by 10, keeping their incidence angle and azimuth fixed, because these are the characteristics that affect the stationary-phase regions (Snieder 2004), contributing to the retrieval of physical arrivals in the SI results. We perform modelling for each of the stations separately, using only those of the selected sources, the arrivals of which reach the station under consideration nearly vertically. In that sense, we perform synthetic modelling, using the same source and receiver distribution as in the real survey, thus having the opportunity to evaluate the acquired results, taking into account both the rough topography and the irregular distribution of the sources. The stations of the Gerolekas passive seismic network that are used for modelling, as well as the number of sources modelled for each station, are presented in Table 1.

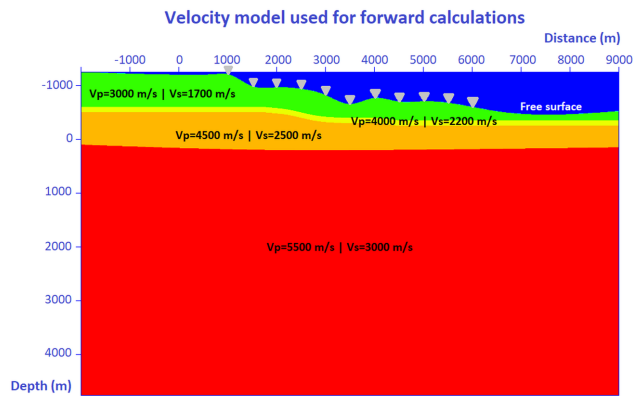
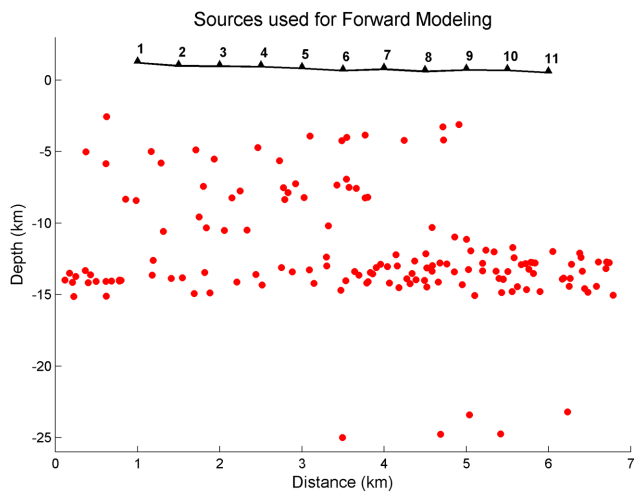


Figure 15  $V_p$  and  $V_s$  distribution, along the cross-section PARV-1, used for 2D elastic forward modelling. The velocity model is built based on geological information and well data, taking into account the original interpretation of the legacy seismic data. Grey triangles represent the stations of the Gerolekas passive seismic network that are located along the line PARV-1.

On the other hand, by placing the sources closer to the receivers, we violate the theoretical assumption of having the sources in the far field of the receivers, which assumption is needed to exchange the requirement of monopole- and dipole-type sources at each source position for only monopole-type





**Figure 16** Positions of the sources used for 2D forward elastic modelling. Black triangles represent the stations of the Gerolekas passive seismic network that are located along the cross-section PARV-1 (receivers of forward modelling), whereas red dots correspond to the microearthquakes that satisfy the verticality criterion for each of the modelled stations (passive sources of forward modelling). Source locations are projected on the seismic line. Each station is modelled separately, using as sources only those of the microearthquakes that produce a signal arriving nearly vertically at the station under consideration.

**Table 1** Stations of the Gerolekas passive seismic network that are used for modelling. For each station, the altitude is provided, as well as the number of sources satisfying the verticality criterion. Locations of these sources are used as input for forward modelling

Modelling Station ID	Gerolekas Network Station ID	Altitude above Mean Sea Level (m)	No. of Sources used for Modelling
1	12	1210	37
2	18	988	32
3	23	965	26
4	29	938	24
5	38	824	16
6	48	655	17
7	55	766	10
8	64	700	8
9	73	705	18
10	82	679	14
11	94	522	9

sources (Wapenaar and Fokkema 2006). Non-compliance with this assumption will result in wrong amplitudes of the retrieved physical arrivals, but also in the retrieval of artefacts. This puts the evaluation of our field results under extra test, which is not present with our field data.

Once our sources and receivers are defined, we perform 2D finite-difference elastic modelling for each station. Because for microearthquakes of that magnitude, the typical characteristics of a double-couple source mechanism are usually either inexistent or negligible, we simulate the sources' signal using a simple force source and a Ricker wavelet. The frequency content of the synthetic signals is selected similar to the real data, with a maximum frequency of 45 Hz and a peak frequency of 20 Hz. Moreover, the model's boundaries, apart from the free surface along the topography, are modelled as absorbing boundaries, by applying a taper on the particle-velocity components both in the  $x$  and  $z$  direction, in order to avoid artificial edge effects.

Using the modelled responses at each station from each of its pertaining sources, we calculate their autocorrelation functions. We then stack the resulting autocorrelograms to retrieve synthetic zero-offset virtual reflection responses below each of the modelled stations. The zero-offset virtual reflection responses retrieved by the signals recorded at the vertical component of the modelled receivers are presented in Figure 17 (top). The modelled signals are emitted by vertical force sources located at the selected hypocentral locations.

In order to facilitate the evaluation of the modelling results, we calculate the two-way travel-times corresponding to the interfaces of the conceptual  $V_p$  model of Figure 15 and add them on the time section of Figure 17 (bottom). For visualization purposes, we denote the bottom of each layer using marks of the same colour as the corresponding layer in Figure 15. More specifically, green marks correspond to the interface between the green layer (flysch) and the upper part of the thin yellow layer in Figure 15 (limestone), yellow marks correspond to the interface between the yellow and the orange limestone layer, whereas orange marks delineate the interface between the orange and the red limestone layer of the conceptual model. The blue marks in Figure 17 (bottom) correspond to the zero-time of each virtual reflection response before removal of the source signature, thus delineating the free surface.

Observing Figure 17 (bottom), we note that all the events corresponding to detectable interfaces of the conceptual model are successfully retrieved by application of SI by autocorrelation on the synthetic data. The results are satisfactory, even for the traces where we expected to have limited illumination, due to the small number of available sources (traces 7, 8 and 11, see Table 1). However, the existence of artefacts due to not tapering the lateral ends of the source distribution for each receiver and due to non-compliance with the far-field assumption makes the interpretation of some of the

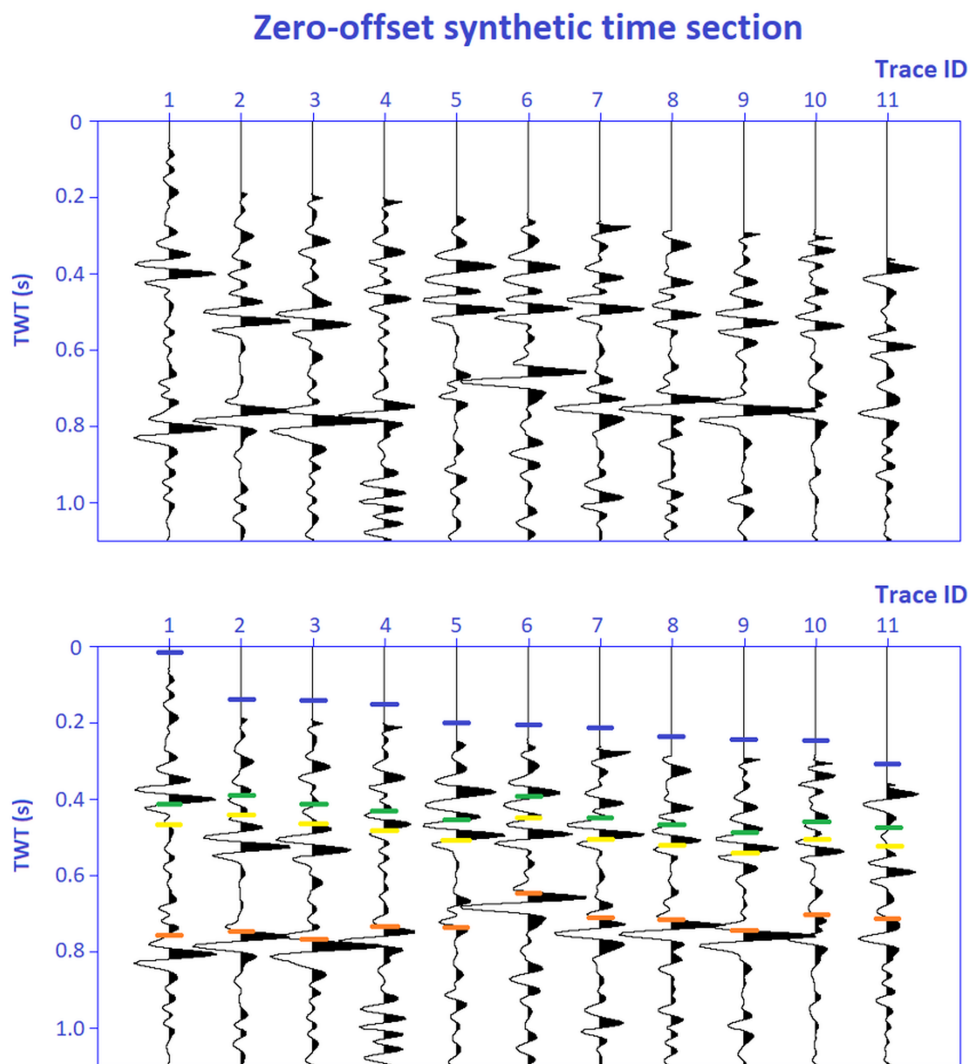


**Figure 17** Zero-offset synthetic virtual reflection responses along the line PARV-1. (Top) Two-way travel-time (TWT) section obtained from the summation of the autocorrelograms of the signals calculated using finite-difference modelling. (Bottom) The same time section but with the calculated expected TWT of the reflectors indicated by the green, yellow and orange, corresponding to the colours of the top three layers in Figure 15. The blue marks show the zero time of each virtual reflection response before removal of the source signature, that is delineate the free surface.

reflectors challenging. This is the case of the green marks at traces 7 and 8, for example. A further challenge for the interpretation comes from the inhomogeneous source distribution below some of the receivers. For example, the sources under station at 1000 m lateral position (trace 1) are mainly present at its right side. This would result in incomplete constructive interference inside the stationary-phase region and thus in the retrieval of a reflection with an erroneous phase. A wrong phase would lead to misinterpretation of the exact depth of the reflectors, for example in underestimation (in the case of trace 1) or overestimation (in the case of traces 2 and 3).

Another observation is that no apparent mode-conversion artefacts exist in the retrieved zero-offset virtual reflection response. This was expected as the careful selection of the sources used for processing, exploiting only those of the recorded microearthquakes satisfying the verticality criterion and sacrificing quantity over quality, ensures little converted energy. Besides, having in mind that we select for modelling stations where a limited number of microearthquakes was recorded (e.g. stations 64 and 94 of the Gerolekas passive seismic network, see Fig. 8), we conclude that even this limited illumination is adequate to reconstruct the subsurface by

application of SI by autocorrelation using the P-wave coda of local microearthquakes.

In addition to this thorough evaluation using forward modelling, we further evaluate the acquired results using the legacy seismic section PARV-1 (Fig. 3). According to the interpretation performed by Hellenic Petroleum in 2004, as depicted in Figure 3, the shallower horizon (yellow line) delineated on the seismic section PARV-1 extends from the depth of 300 m above mean sea level at the northern part of the line to a depth of 200 m above mean sea level towards the South. The second interpreted horizon (blue line) is also located at 300 m above mean sea level at the northern end of the seismic line, extending down to mean sea level along the line, to end at a depth of 100 m above mean sea level in the southern part. Both lines seem to be interrupted by the presence of two faults located at the shot points 350 and 400. The deepest interpreted horizon (red line) extends slightly below mean sea level (from mean sea level to approximately 100 m below mean sea level).

In order to evaluate the results acquired by our passive SI approach, we first create a comparable image, by extracting the virtual reflection response of the vertical component down to the depth of 1200 m below mean sea level from the depth-converted cross-section of Figure 14. We detect interpretable reflectors around the depths of interest and delineate them using the same colours as in the legacy migrated depth section (yellow, blue and red). The interpreted SI depth section is presented in Figure 18.

Observing the depth section of Figure 18 (top), one can see the three reflectors delineated on the PARV-1 seismic line. Although the interpretation provided back in 2004 is quite ambiguous, due to the poor quality of the legacy data, and an alternative interpretation could be proposed by the SI results, all three reflectors can be detected in the acquired zero-offset depth section. The only major difference is the absence of the interruption located near the shot point 400, which was interpreted as a fault, and was expected to be delineated near the position of the virtual reflection trace 16. However, we explain this absence by the coarser character of the passive SI results, mainly in terms of horizontal spatial resolution. Having in mind that every virtual shot point corresponds to approximately 40 shot points of the active seismic survey, this fact cannot be attributed to a pitfall of the methodology itself. It rather underlines the need for a denser coverage of the area of interest by recording stations.

After evaluating the virtual reflection response along the line PARV-1, using the three known reflectors delineated on the legacy migrated depth section, we attempt to pinpoint a

number of additional reflectors that are visible on the SI result. These reflectors are marked with magenta lines on the cross-section of Figure 18 (bottom). Although clear reflectors are visible both above and below the deepest interpreted horizon from seismic (red line), for the moment we limit our interpretation only to the shallower part. This is dictated by the interest of the mining company down to about mean sea level. In the shallower part of our results, we can easily delineate clearly interpretable reflectors (magenta lines). Note that at those shallow depths the legacy active seismic section was suffering from severe masking effects. We do not attempt to link the interpreted reflectors to geological formations, as the thorough interpretation of the Gerolekas passive SI results extends beyond the scope of the present work. By delineating them, we just aim to validate the potential of the application of passive SI in the context of mineral exploration.

Last, but not least, the obtained SI vertical depth section along the seismic line PARV-1, the orientation of which is approximately North–South, is presented in Figure 19, along with an East–West–oriented section acquired by applying the same processing workflow. By this, we aim to examine the continuity of the retrieved events in space. Observing Figure 19, it becomes evident that there is an undeniable consistency of the retrieved reflectors along both directions, which, taking into account the 1D character of the applied processing procedure, further validates the quality of the acquired results.

## DISCUSSION

We applied reflected-wave passive seismic interferometry (SI), using body waves from local microearthquakes, in the context of the Gerolekas mining exploration survey. Our results showed that this methodology can provide valuable information on the subsurface, even at an exploration scale.

Using a dense seismological network of 129 three-component short-period stations for data acquisition, installed at inter-station distances of approximately 500 m and recording for a period of 4 months, as well as a sophisticated event detection and picking algorithm, we achieved the detection and location of a significant number of local microearthquakes of very small magnitude. This fact provided us a means of overcoming the intrinsic limitation of reflected-wave passive SI, concerning the difficulty of detecting and extracting useful body-wave signal from any passive seismic record.

In addition to that, the use of three-component recordings permitted us the extraction of the virtual reflection responses

## Zero-offset depth sections

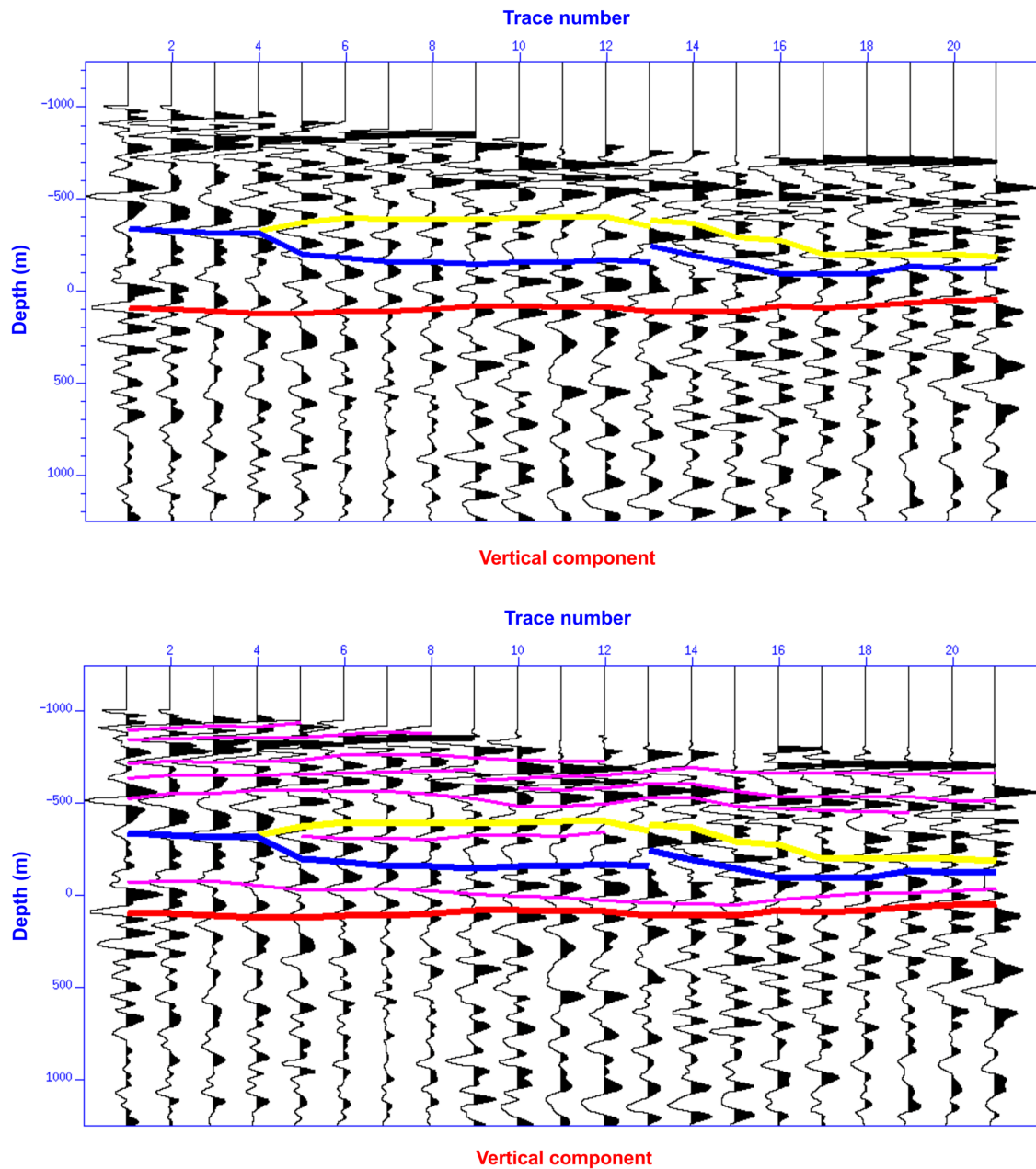


**Figure 18** Zero-offset depth section of the virtual reflection responses (vertical component) along the seismic line PARV-1. The cross-section extends from the surface (datum at 1200 m above mean sea level) down to a depth of 1200 m below mean sea level (similarly to the PARV-1 seismic line). The three major reflectors interpreted on the seismic line PARV-1 are delineated on the cross-section (top), whereas additional shallow, clearly interpretable reflectors are marked in magenta lines (bottom).

for both P- and S-waves. Comparing the P- and S-wave sections in Figure 14, we see that there are reflectors consistent in all three components. We also see that the S-wave sections provide higher vertical resolution. This is logical due to the

shorter wavelength of the S-waves and the same frequency band of interest. On the other hand, this is not necessarily expected, because the S-wave coda window, used for auto-correlation, contains also P-wave arrivals. Such arrivals might

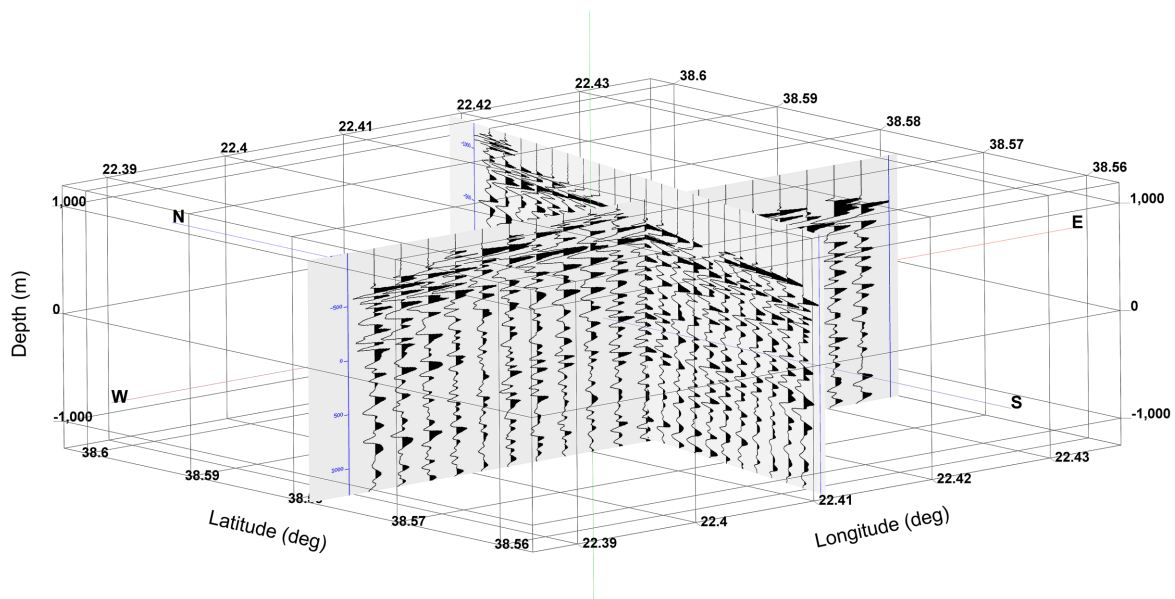


Figure 19 Zero-offset depth section of the virtual reflection responses (vertical component) along the seismic line PARV-1 (North–South-oriented) and an East–West-oriented section. Both sections extend from the surface down to a depth of 1200 m below mean sea level. Continuity of the retrieved reflectors can be observed along both directions.

give rise to retrieved spurious events. It appears, though, that the summation of the available microearthquakes per station has sufficiently suppressed such spurious energy.

From the comparison in Figure 14, we also notice features that appear only on one or both of the horizontal components. To understand these differences, a thorough interpretation of the acquired results is needed, which extends beyond the scope of this preliminary work.

The fact that we accurately located the microearthquakes used as input for passive SI and picked their P- and S-wave onset times permitted a more precise definition of the duration of their P- and S-wave coda. This enabled us to apply the methodology both for P- and for S-waves, despite the very small magnitude of the involved events, using much more robust input signals than the ones usually employed at this scale.

The retrieved virtual reflection responses exhibit numerous reflectors that could be delineated on both the vertical and the horizontal components' cross-sections. There seems to be useful signal down to a depth exceeding 5 km. However, our most important observation is the fact that there are clear reflectors delineated from the surface down to the first few hundreds of metres, at the zone where reflection seismology usually suffers from the presence of surface waves, refracted waves and near-surface effects. It is worth noting here that the nature itself of the signal used to calculate virtual reflection

responses (P- and S-wave coda of local microearthquakes), as well as the technique applied, precludes retrieval of surface and refracted waves. This can be seen as a data-driven near-perfect filter for such waves.

We thoroughly evaluated the acquired results by applying two-dimensional (2D) finite-difference modelling, simulating the Gerolekas survey's difficult conditions, as realistically as possible. We confirmed the applicability of the proposed methodology, using sources as in the field survey, both in terms of number and incidence angles and in terms of frequency content of the signals. We showed that, even in the cases of stations where a limited number of microearthquakes were satisfying the verticality criterion set during the selection of our sources, we managed to retrieve interpretable reflectors at the depths of interest. Moreover, we confirmed the absence of mode-conversion artefacts in the retrieved virtual reflection responses, underlining the importance of carefully selecting sources that are limited inside the stationary-phase region of vertical incidence for each station.

The acquired results could further be improved if we used a three-dimensional (3D) velocity distribution for the time-to-depth conversion, instead of an average one-dimensional velocity model. This model could be calculated by applying local earthquake tomography on the same dataset, using the first arrivals of the recorded earthquakes. Actually, this is the ultimate scope of the Gerolekas passive seismic

survey – jointly exploiting information derived from the application of different passive seismic methodologies on the same dataset.

Last, but not least, the single-station approach of calculating autocorrelations of the recorded signals presented here could be extended to 2D/3D, if the inter-station distances were such that would permit cross-correlating the signals without introducing any aliasing effects. This would provide more sophisticated imaging of the subsurface, as well as an improved horizontal resolution of the results acquired.

## CONCLUSIONS


We applied passive seismic interferometry (SI) using body waves of local microearthquakes to retrieve reflected waves at the exploration scale. We implemented the methodology to 4-month-long passive recordings from the Gerolekas bauxite mining site, Central Greece. We applied SI by autocorrelation to microearthquakes selected to have their first arrivals characterized by near vertical emergence at a station. This ensured retrieval of zero-offset reflection responses from a virtual source emitting energy vertically down. We retrieved both P- and S-wave subsurface sections. We evaluated the acquired results by forward modelling, proving that we can successfully retrieve interpretable reflectors, using the same source and receiver scheme as in the field survey and we confirmed the absence of mode-conversion artefacts in the obtained virtual reflection responses. Comparing the depth section from legacy active-source data to a P-wave zero-offset depth section from the SI results formed along the line of the legacy data, we showed that we successfully imaged three subsurface reflectors interpreted in the active data. We further could image shallower reflectors that were not detectable in the legacy active data. The results of the SI methodology we applied showed that passive seismic imaging with local microearthquakes can provide an innovative and cost-effective exploration alternative to active-source data, especially in cases where traditional approaches reach their limits. The environmentally friendly character of our methodology, as well as its ease of implementation, makes it applicable even in extremely prohibiting conditions, in terms of accessibility or permitting.

## ACKNOWLEDGEMENTS

The Gerolekas passive seismic survey was launched in the context of the Smart Exploration action, funded by the European Commission, in the framework of the H2020 ‘New solutions for sustainable production of raw materials – New

sensitive exploration technologies’. Smart Exploration has received funding from the European Union’s Horizon 2020 research and innovation programme under grant agreement No. 775971. The authors would like to thank Seismotech S.A. for acquiring the Gerolekas passive seismic dataset, as well as for their valuable input on the analysis of the continuous passive seismic data. We also thank Delfi-Distomon S.A. for sharing all available well and seismic information of the study area, as well as two anonymous reviewers for their constructive comments that helped improve this manuscript.

## ORCID

Katerina Polychronopoulou   
<https://orcid.org/0000-0002-7676-6243>

## REFERENCES

- Abe S., Kurashimo E., Sato H., Hirata N., Iwasaki T. and Kawanaka T. 2007. Interferometric seismic imaging of crustal structure using scattered teleseismic waves. *Geophysical Research Letters* **34**, L19305.
- Almagro Vidal C., Draganov D., van der Neut J., Drijkoningen G. and Wapenaar K. 2014. Retrieval of reflections from ambient-noise field data using illumination diagnosis. *Geophysical Journal International* **198**, 1572–1584.
- Aronis G.A. 1955. Geographical distribution, geological placing and aspects on the genesis of the Greek bauxites. *Bulletin of the Geological Society of Greece* **2**, 55–79.
- Benardos A. and Katopodis D. 2011. Design of an underground bauxite exploitation in Greece. Proc. Mine Planning and Equipment Selection Symposium MPES 2011, Almaty, Kazakhstan, 115–126.
- Boullenger B., Verdel A., Paap B., Thorbecke J. and Draganov D. 2015. Studying CO<sub>2</sub> storage with ambient-noise seismic interferometry: a combined numerical feasibility study and field-data example for Ketzin, Germany. *Geophysics* **80**, Q1–Q13.
- Cheraghi S., Craven A.J. and Bellefleur G. 2015. Feasibility of virtual source reflection seismology using interferometry for mineral exploration: a test study in the Lalor Lake VMS mining area, Manitoba, Canada. *Geophysical Prospecting* **63**, 833–848.
- Claerbout J. 1968. Synthesis of a layered medium from its acoustic transmission response. *Geophysics* **33**, 264–269.
- Daneshvar M.R., Clarence C.S. and Savage M.K. 1995. Passive seismic imaging using microearthquakes. *Geophysics* **60**, 1178–1186.
- Draganov D., Campman X., Thorbecke J., Verdel A. and Wapenaar K. 2009. Reflection images from ambient seismic noise. *Geophysics* **74**, A63–A67.
- Draganov D., Campman X., Thorbecke J., Verdel A. and Wapenaar K. 2013. Seismic exploration-scale velocities and structure from ambient-seismic noise (>1 Hz). *Journal of Geophysical Research* **118**, 1–16.

- Draganov D., Wapenaar K., Mulder W., Singer J. and Verdel A. 2007. Retrieval of reflections from seismic background-noise measurements. *Geophysical Research Letters* **34**, L04305.
- Leontarakis K., Lois A., Pantazopoulos A. and Polychronopoulou K. 2015. A comprehensive methodology for automated analysis of seismic records and its contribution to a passive seismic tomography survey in Delvina, SW Albania. 85th SEG meeting, New Orleans, USA, Expanded Abstracts, 18–23.
- Lois A., Sokos E., Martakis N., Paraskevopoulos P. and Tselentis G-A. 2013. A new automatic S-onset detection technique: application in local earthquake data. *Geophysics* **78**, KS1–KS11.
- Ljung, L. 1987. *System Identification: Theory for the User*. Upper Saddle River, NJ: Prentice-Hall.
- Minato S., Matsuoka T., Tsuji T., Draganov D., Hunziker J. and Wapenaar K. 2011. Seismic interferometry using multidimensional deconvolution and crosscorrelation for crosswell seismic reflection data without borehole sources. *Geophysics* **76**, SA19–SA34.
- Nakata N., Snieder R. and Behm M. 2014. Body-wave interferometry using regional earthquakes with multidimensional deconvolution after wavefield decomposition at free surface. *Geophysical Journal International* **199**, 1125–1137.
- Nakata N., Snieder R., Tsuji T., Larner K. and Matsuoka T. 2011. Shear wave imaging from traffic noise using seismic interferometry by cross-coherence. *Geophysics* **76**, SA97–SA106.
- Nishitsuji Y., Ruigrok E., Gomez M., Wapenaar K. and Draganov D. 2016a. Reflection imaging of aseismic zones of the Nazca slab by global-phase seismic interferometry. *Interpretation* **4**, SJ1–SJ16.
- Nishitsuji Y., Rowe C., Wapenaar K. and Draganov D. 2016b. Reflection imaging of the moon's interior using deep moonquake seismic interferometry. *Journal of Geophysical Research: Planets* **121**, 695–713.
- Oren C. and Nowack R.L. 2017. Seismic body-wave interferometry using noise autocorrelations for crustal structure. *Geophysical Journal International* **208**, 321–332.
- Panea I., Draganov D., Almagro Vidal C. and Mocanu V. 2014. Retrieval of reflections from ambient noise recorded in Mizil area, Romania. *Geophysics* **79**, Q31–Q42.
- Perron V., Laurendeau A., Hollender F., Bard P-Y., Gelis C., Traversa P. et al. 2018. Selecting time windows of seismic phases and noise for engineering seismology applications: a versatile methodology and algorithm. *Bulletin of Earthquake Engineering* **16**, 2211–2225.
- Polychronopoulou K., Orfanos C., Martakis N. and Draganov D. 2019. Preliminary results of an integrated passive seismic survey at the Gerolekas bauxite mining site – Central Greece. EAGE Near Surface Geoscience 2019, The Hague, Extended Abstracts.
- Romero P. and Schimmel M. 2018. Mapping the basement of the Ebro Basin in Spain with seismic ambient noise autocorrelations. *Journal of Geophysical Research: Solid Earth* **123**, 5052–5067.
- Ruigrok E., Campman X. and Wapenaar K. 2011. Extraction of P-wave reflections from microseisms. *Comptes Rendus Geoscience* **343**, 512–525.
- Ruigrok E. and Wapenaar K. 2012. Global-phase seismic interferometry unveils P-wave reflectivity below the Himalayas and Tibet. *Geophysical Research Letters* **39**, L11303.
- Saragiotis C.D., Hadjileontiadis L.J. and Panas S.M. 2002. PAI-S/K: a robust automatic seismic P phase arrival identification scheme. *IEEE Transactions on Geoscience and Remote Sensing* **40**, 1395–1404.
- Scherbaum F. 1987. Seismic imaging of the site response using microearthquake recordings, Part II – application to the Swabian Jura, southwest Germany, seismic network. *Bulletin of the Seismological Society of America* **77**, 1924–1944.
- Schuster G.T., Yu J. and Rickett J. 2004. Interferometric/daylight seismic imaging. *Geophysical Journal International* **157**, 838–852.
- Snieder R. 2004. Extracting the Green's function from the correlation of coda waves: a derivation based on stationary phase. *Physical Review E* **69**, 046610–1–046610-8.
- Stockwell Jr. J.W. and Cohen J.K. 2008. CWP/SU: Seismic Un\*x Release No. 44R14: an open source software package for seismic research and processing. Center for Wave Phenomena, Colorado School of Mines.
- Thorbecke J. and Draganov D. 2011. Finite-difference modeling experiments for seismic interferometry. *Geophysics* **76**, H1–H18.
- Wadati K. 1933. On the travel time of earthquake waves, Part II. *Geophysical Magazine* **7**, 113–137.
- Wapenaar K. 2004. Retrieving the elastodynamic Green's function of an arbitrary inhomogeneous medium by cross correlation. *Physical Review Letters* **93**, 254301.
- Wapenaar K., Draganov D., Snieder R., Campman X. and Verdel A. 2010. Tutorial on seismic interferometry: part1 – Basic principles and applications. *Geophysics* **75**, 75A195–75A209.
- Wapenaar K. and Fokkema J. 2006. Green's functions representations for seismic interferometry. *Geophysics* **71**, SI33–SI46.